Rheol Acta (2004) 43: 17–37
DOI 10.1007/s00397-003-0317-8

ORIGINAL CONTRIBUTION

M.Gregory Forest
Qi Wang
Ruhai Zhou

The weak shear kinetic phase diagram for nematic polymers

Received: 11 March 2003
Accepted: 21 May 2003
Published online: 5 September 2003

M.G. Forest (✉) · R. Zhou
Department of Mathematics,
University of North Carolina at Chapel Hill,
Chapel Hill, NC27599, USA
E-mail: forest@amath.unc.edu

Q. Wang
Department of Mathematical Sciences,
Florida State University, Tallahassee,
FL32306, USA

Abstract We study the shear problem for nematic polymers as modeled by the molecular kinetic theory of Doi (1981), focusing on the anomalous slow flow regime. We provide the kinetic phase diagram of *monodomain* (MD) *attractors* and *phase transitions* vs normalized nematic concentration (N) and weak normalized shear rate (Peclet number, Pe). We then overlay all rheological features typically reported in experiments: alignment properties, normal stress differences and shear stress. These features play a critical role in the synthesis between theory and experiment for nematic polymers (Larson 1999; Doi and Edwards 1986). MD *type* is routinely used for rheological shear characterization: cf., flow-aligning 5CB (Mather et al. 1996a), tumbling PBT (Srinivasarao and Berry 1991), and 8CB (Mather et al. 1996b), evidence for a wagging regime (Mewis et al. 1997), out-of-plane kayaking modes (Larson and Ottinger 1991), and evidence for chaotic major director dynamics (Bandyopadhyay et al. 2000). MD *transitions* correlate with sign changes in normal stresses (Larson and Ottinger 1991; Magda et al. 1991; Kiss and Porter 1978, 1980). Furthermore, structure formation in shear devices appears to be correlated with monodomain precursor dynamics (Tan and Berry 2003; Forest et al. 2002a). In this paper we combine seminal kinetic theory results (Kuzuu and Doi 1983, 1984; Larson 1990; Larson and Ottinger 1991; Faraoni et al. 1999; Grosso et al. 2001), symmetry observations (Forest et al. 2002b), and mesoscopic results on the fate of orientational degeneracy in weak shear (Forest and Wang 2003; Forest et al. 2003a), together with our resolved numerical simulations, to provide the kinetic flow-phase diagram of Doi theory in the weak shear regime, $0 < Pe < 1$, for infinitely thin rods. We report the "birth" of key rheological features at the onset of flow: *sign changes and local maxima and minima in normal stress differences (N_1 and N_2) associated with MD transitions*. These results serve as the basis for continuation of the kinetic phase diagram to $Pe > 1$; as the definitive benchmark for any mesoscopic or continuum model; and experimental data can be compared in order to determine accuracy and limitations of the Doi theory in weak shear.

Keywords Nematic polymer · Kinetic · Shear flow · Phase diagram · Rheology

Introduction

Larson (1990), Larson and Ottinger (1991), Faraoni et al. (1999), and Grosso et al. (2001) have identified monodomain (MD) attractors of the Doi kinetic theory for rigid nematic polymers in various regimes of normalized concentration N and shear-rate Pe: flow-aligning (**FA**), tumbling and wagging (**TW**), kayaking ($\mathbf{K}_1$ and $\mathbf{K}_2$), out-of-plane steady (**OS**), log-rolling (**LR**), and chaotic (**CH**). Furthermore, all of these rheological response modes have been observed in shear experiments with nematic polymers (cf. Larson 1999 and the extensive review of Tan and Berry 2003). Forest and Wang (2003) showed that all these attractors are captured with standard moment-closure models associated with the "parent" Doi kinetic equation if one allows variable molecular aspect ratio and varies the closure rule, yet no single closure rule is successful in reproducing all stable monodomains and transition behavior. It is clear that one has to appeal to the kinetic equation to distinguish artifacts of the second-moment truncation if one is to have a *definitive solution space vs molecular and flow parameters of modern kinetic theory*.

A resolved phase diagram of kinetic theory for nematic polymers and all rheological properties associated with MD attractors and phase transitions in weak shear are the goals of this paper. Seminal kinetic analyses of Kuzuu and Doi (1983, 1984), Semenov (1983), Archer and Larson (1995), Kroger and Sellers (1995) and results for the dilute concentration regime (See et al. 1990; Forest et al. 2003b) serve as guides for theory and computation. Continuum Leslie-Ericksen theory is recoverable from kinetic theory under a highly restrictive list of flow and molecular assumptions: weak shear limit, very high concentrations, small molecular weight. It is clear that nematic polymers require the more general Doi theory; the extent to which second-moment closure approximations of kinetic theory are sufficient to model sheared nematic polymers has occupied significant attention (Advani and Tucker 1987; Chaubal et al. 1995; Beris and Edwards 1994; Wang 1997; Chaubal and Leal 1998). The authors (Forest and Wang 2003; Forest et al. 2003a) extended these seminal kinetic analyses to any mesoscopic tensor model, a much simpler context from which one can exactly solve the weak flow limit while retaining dependence upon concentration N and molecular shape parameter a . One can analytically identify consequences for MD attractors and transitions that are *due to closure rule* and not from molecular and flow physics; e.g., the mesoscopic analog of the continuum Leslie tumbling parameter is strongly closure-dependent (Forest et al. 2003c). On the other hand, several features in weak shear are robust to closure (flow-aligning at dilute concentrations N, an unsteady intermediate range of concentrations, and steady vorticity alignment for $N \gg 1$), which provide a skeleton for the complete picture.

In this paper, we give *the kinetic phase diagram of Doi theory for* $0 < Pe < 1$ *and arbitrary concentration* N. We proceed to provide rheological properties of all attractors (alignment, birefringence and stress data); the correlations between attractor phase transitions, sign changes in N_1, N_2, and structure properties of shear stress. These results stand as the benchmark in weak shear for any closure approximation or mesoscopic model, and as the experimental benchmark from which to test the Doi kinetic theory for a given nematic polymer.

The details of the kinetic phase diagram are inherently complex because prior to flow, quiescent nematic polymers are orientationally degenerate as eloquently discussed by Marrucci and Greco (1993). This degeneracy corresponds to an $O(3)$ symmetry of every orbit of the kinetic Smoluchowski equation except the lone isotropic equilibrium (Forest et al. 2002b). Weak shear breaks this symmetry leading to quite subtle and variable stationary distributions (both steady and oscillatory) vs N and Pe.

The first resolved kinetic theory simulations of Marrucci and Maffettone (1989), Larson (1990), and Larson and Ottinger (1991) established that the Doi theory successfully predicts shear-rate dependent transitions (tumbling to wagging to steady alignment) and associated sign change in averages of N_1. Furthermore, these results were not sensitive to the particular form of the mean-field, excluded-volume potential. Faraoni et al. (1999) and Grosso et al. (2001) have used numerical bifurcation software (AUTO) together with spherical harmonic expansions to determine monodomain attractors and transition curves for selected regions of the parameter space (N,Pe). We complement their studies by a combined mesoscopic-microscopic strategy, focusing on the anomalous slow flow regime for this paper.

This approach is an example of the general conceptual numerical framework advocated by Kevrekidis (Theodoropoulos et al. 2000; Gear et al. 2003). Analysis and numerical results from moment-closure models (Forest and Wang 2003; Forest et al. 2003a) are used as a predictor. We then employ kinetic simulations to confirm the robust features of mesoscopic predictions, and to resolve and remove sensitivity associated with closure approximations, giving the full phase diagram for all N and $0 < Pe < 1$. Rheological implications are then provided only for stable MDs and across phase transition boundaries.

The Doi kinetic theory

We recall the basic elements of the Doi kinetic theory for nematic polymers in simple shear flows. In order to make explicit contact with the results of Faraoni et al.

(1999) and Grosso et al. (2001), we restrict ourselves to rigid rods of infinite aspect ratio. Let $f(\mathbf{m},t)$ be the *orientational probability distribution function* (PDF) for molecules with axis of symmetry $\mathbf{m}$ on the unit sphere S^2. The Smoluchowski (kinetic) equation for $f(\mathbf{m},t)$ in a flow field $\boldsymbol{v}$ is given by (Doi 1981; Hess 1976)

$$\frac{Df}{Dt} = \mathcal{R}\cdot\left[D_r(\mathbf{m})\left(\mathcal{R}f + \frac{1}{kT} f \mathcal{R} V\right)\right] - \mathcal{R}\cdot[\mathbf{m}\times\dot{\mathbf{m}} f] \tag{1}$$

$$\dot{\mathbf{m}} = \Omega\cdot\mathbf{m} + [\mathbf{D}\cdot\mathbf{m} - \mathbf{D}:\mathbf{mmm}]$$

where $D_r(\mathbf{m})$ is the rotary diffusivity which we hold constant, $D_r(\mathbf{m}) = D_r^0$, again to make contact with Faraoni et al. (1999) and Grosso et al. (2001); k is the Boltzmann constant; T is absolute temperature; $\mathcal{R} = \mathbf{m}\times\frac{\partial}{\partial\mathbf{m}}$ is the rotational gradient operator (Bird et al. 1987); and $\frac{D}{Dt}()$ denotes the material derivative $\frac{\partial}{\partial t}() + \mathbf{v}\cdot\nabla()$. For this paper we consider simple shear flow $\mathbf{v}$ given in Cartesian coordinates (x,y,z) with shear rate γ by

$$\mathbf{v} = \dot{\gamma}(\mathrm{y}, 0, 0), \tag{2}$$

from which $\mathbf{D}$ and Ω are the corresponding rate-of-strain and vorticity tensors,

$$\mathbf{D} = \frac{1}{2}\dot{\gamma}\begin{pmatrix} 0 & 1 & 0 \\ 1 & 0 & 0 \\ 0 & 0 & 0 \end{pmatrix}, \Omega = \frac{1}{2}\dot{\gamma}\begin{pmatrix} 0 & 1 & 0 \\ -1 & 0 & 0 \\ 0 & 0 & 0 \end{pmatrix}. \tag{3}$$

The Peclet number, $Pe = \dot{\gamma}/D_r^0$, is the normalized shear-rate parameter, which we limit to the weak range $0 \le Pe \le 1$. In Eq. (1), the second-moment of the PDF f,

$$\mathbf{M} = \langle\mathbf{mm}\rangle = \int_{\|\mathbf{m}\|=1} \mathbf{mm} f(\mathbf{m},t) d\mathbf{m}, \tag{4}$$

enters through the mean-field, Maier-Saupe excluded-volume potential V,

$$V = -\frac{3}{2} NkT\mathbf{mm} : \mathbf{M}, \tag{5}$$

where N is the dimensionless strength of the potential V, proportional to the concentration of rods. The *mesoscopic orientation tensor* $\mathbf{Q}$ is the traceless part of $\mathbf{M}$,

$$\mathbf{Q} = \mathbf{M} - \frac{1}{3}\mathbf{I}, \tag{6}$$

whose entries are measurable in the laboratory; e.g., see Fuller (1995) and Burghardt (1998), and which allow comparisons with rheo-optical measurements of principle axes of bulk molecular alignment as well as birefringence. These mesoscopic properties are deduced from all kinetic distribution functions and imaged in the figures below. Additionally, the stress tensor (Appendix, Eq. A3) associated with each MD attractor is calculated, and measurable normal stress differences and shear stresses are given across the phase diagram.

Spherical harmonic expansion and second-moment projection of *f*

Let θ,ϕ be spherical coordinates with θ the polar angle measured from the vorticity axis (z) and ϕ the latitude angle in the shear plane (x,y), measured counter-clockwise from the positive flow direction (x); y is the flow-gradient direction. The molecule axis $\mathbf{m}\in S^2$ is then represented by

$$\mathbf{m} = (\sin\theta\cos\phi, \sin\theta\sin\phi, \cos\theta) \tag{7}$$

As in Larson (1990), Larson and Ottinger (1991), Faraoni et al. (1999), and Grosso et al. (2001), we seek solutions of Eqs. 1, 2, 3, 4, 5, 6 in the form of a spherical harmonic expansion,

$$f(\mathbf{m},t) = \sum_{l=0}^{L}\sum_{m=-l}^{l} a_{l,m}(t) Y_l^m(\theta,\phi) \tag{8}$$

where Y_l^m are complex spherical harmonic functions (Messiah 1961),

$$Y_l^m = P_l^m(\cos\theta) e^{im\phi} \tag{9}$$

P_l^m are Legendre polynomials, and L is the order of truncation in the Galerkin approximation. The projection of f onto its traceless second moment $\mathbf{Q}$ is explicitly given by

$$\begin{aligned} Q_{xx} &= -\tfrac{2}{3}\sqrt{\tfrac{\pi}{5}} a_{2,0} + \sqrt{\tfrac{8\pi}{15}} Re(a_{2,2}) \\ Q_{yy} &= -\tfrac{2}{3}\sqrt{\tfrac{\pi}{5}} a_{2,0} - \sqrt{\tfrac{8\pi}{15}} Re(a_{2,2}) \\ Q_{xy} &= -\sqrt{\tfrac{8\pi}{15}} Im(a_{2,2}) \\ Q_{xz} &= -\sqrt{\tfrac{8\pi}{15}} Re(a_{2,1}) \\ Q_{yz} &= \sqrt{\tfrac{8\pi}{15}} Im(a_{2,1}), \end{aligned} \tag{10}$$

where $Re(\cdot)$ and $Im(\cdot)$ represent real and imaginary parts, respectively. In simulations below, we project $f(\mathbf{m},t)$ onto its second moment, $\mathbf{Q}(f(\mathbf{m},t))$ or $\mathbf{M}(f(\mathbf{m},t))$, which allows the explicit kinetic prediction of measurable experimental data. The eigenvalues of $\mathbf{M}$ are ordered $0 \le d_3 \le d_2 \le d_1 \le 1$ ($\mathbf{Q}$ has eigenvalues $d_i - \frac{1}{3}$; $\mathbf{Q}$ and $\mathbf{M}$ share a basis of orthogonal eigenvectors $\mathbf{n}_1,\mathbf{n}_2,\mathbf{n}_3$. This defines the *major director* for $f(\mathbf{m},t)$, given by the direction $\mathbf{n}_1$ of maximum degree d_1 of mesoscopic alignment. The order parameters convey birefringence, d_i–d_j, in the principal orientation planes defined by the directors. Finally, all stress data is derived from the PDF projections onto $\mathbf{Q}$ and the fourth-moment. The stress tensor is given in the Appendix.

The weak shear problem

Figure 1 depicts the equilibrium ($\mathbf{v}=\mathbf{0}$) isotropic-nematic phase diagram (de Gennes and Prost 1993; Faraoni et al. 1999; Grosso et al. 2001). This standard representation of the isotropic $\left(d_i=\frac{1}{3};\ i=1,2,3\right)$ and nematic equilibria f_* of (1) arises by projection of f_* onto the second-moment $\mathbf{Q}(f_*)$ (Eq. 10), which are all uniaxial ($d_i=d_j$ for at least two $i\neq j$) for the Maier-Saupe potential (de Gennes and Prost 1993). Thus $\mathbf{Q}(f_*)$ is specified by the single order parameter $s*=d_1-d_3=\frac{3}{2}\left(d_1-\frac{1}{3}\right)$ of $\mathbf{Q}(f_*)$, plotted in Fig. 1. By design (de Gennes and Prost 1993), this picture removes the underlying $O(3)$ symmetry of the Smoluchowski equation (1) with $\mathbf{v}=0$. *The nematic solution branches, $s_\pm$, correspond to an entire $O(3)$ group of equilibria, and the saddle-node bifurcation at $N\approx 4.49$, marking the birth of the nematic phases, is an $O(3)$ of saddle-nodes*. Furthermore, all initial-value solutions for arbitrary anisotropic initial data $f(\mathbf{m},0)\neq\frac{1}{4\pi}$ are $O(3)$ degenerate, i.e., each orbit $f(\mathbf{m},t)$ generates an entire continuous group of orbits $f(\mathbf{U}\ \mathbf{m},t)$ for all $\mathbf{U}\in O(3)$ (Forest et al. 2002b). The $O(3)$ symmetry projects onto the second-moment tensor in the form $\mathbf{U}^T\ \mathbf{Q}\ \mathbf{U}$ (Forest and Wang 2003), which recovers the fundamental symmetry property of Landau-de Gennes mesoscopic theory (de Gennes and Prost 1993; Beris and Edwards 1994).

This underlying symmetry is broken by any generic perturbation. We refer to Marrucci and Greco (1993) for an inspiring discussion. In the case of weak flows such as shear, the selection mechanisms that determine which stationary orientational distributions persist, either as steady or unsteady states, have remained elusive. Early seminal work is due to Hess (1976), Semenov (1983), Kuzuu and Doi (1983, 1984): Marrucci and Maffettone (1989), Marrucci (1991), and Marrucci and Greco (1991, 1993) which aim to construct stationary distribution functions and to predict scaling properties versus theoretical parameters. One of the first questions to resolve is the *count of how many solutions persist in weak shear vs nematic concentration N, their steady or unsteady character* and *the stability of each state*. Kuzuu and Doi (1983, 1984) developed an asymptotic analysis as $Pe\to 0$ which applies to high N, from which they deduce a kinetic theory analog of the continuum Leslie parameter λ_L. They determine an implicit, molecular-parameter-basis for flow-aligned vs tumbling of nematic polymers. The method does not admit more general selection criteria, such as the number, type, and stability of stationary solutions, and their variability due to changes in concentration N. To gain these predictions along with scaling properties versus Doi theory parameters, the authors (Forest et al. 2003a) projected kinetic theory onto the second-moment tensor, where the Kuzuu-Doi method can be extended and explicitly solved. One conclusion of this analysis is the delineation of features of the flow-phase diagram that are robust vs sensitive to closures, and the need to appeal to kinetic, resolved simulations to clear up closure-sensitive features.

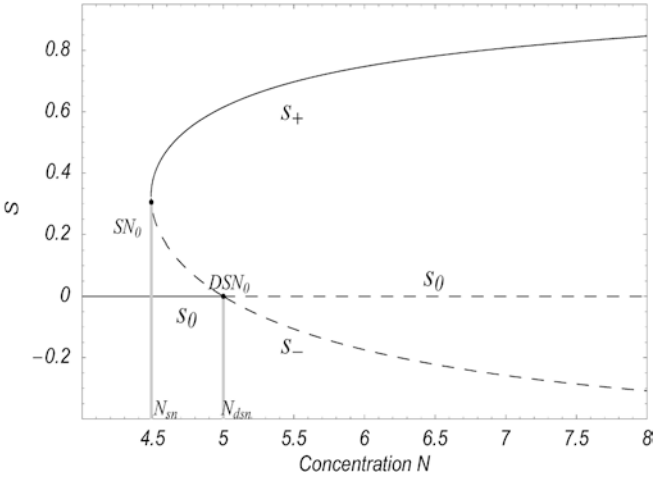

Fig. 1 The isotropic-to-nematic phase diagram for quiescent nematic liquids of infinite aspect ratio of the Smoluchowski equation (Eq. 1) without flow vs nematic concentration N. The *vertical axis* depicts the uniaxial order parameter, s_*, derived from the projection of f_* onto the second-moment tensor $\mathbf{Q}_*$, from which $\frac{2}{3}s_*$ is the simple eigenvalue. *Solid lines* represent stable, *dashed lines* unstable, steady solutions. $f_0=\frac{1}{4\pi}$ is the isotropic state which exists for all N, whose second-moment tensor $\mathbf{Q}_0=\mathbf{0}$ and $s_0=0$; the isotropic equilibrium is isolated, and non-degenerate

To foreshadow our approach, we first look for features of the quiescent diagram that are robust to weak shear perturbations. For example, *saddle-node bifurcations are structurally stable*, so SN_0 of Fig. 1, $N\approx 4.49$, the key bifurcation at which nematic states first arise, will survive in weak shear. The continuous $O(3)$ symmetry of f does not survive shear flow perturbations, rather a discrete reflection symmetry emerges (Forest et al. 2002b). The *discrete, finite multiplicity of SN bifurcations for N nearby 4.49 is a primary structure* to be determined. By contrast, the double saddle-node bifurcation DSN_0 of Fig. 1, where the isotropic state loses stability, is structurally unstable, and will be destroyed by generic perturbations.

Significant understanding of the shear problem for nematic polymers has come from numerical simulations of kinetic theory, beginning with Marrucci and Maffettone (1989), Larson (1990), and Larson and Ottinger (1991) and continuing over the past decade. The most complete results, covering targeted regions of the (N,Pe) parameter space, are given by Faraoni et al. (1999) and Grosso et al. (2001); our purpose here is to elucidate further the *selection mechanisms in the weak shear limit*, and to progress further toward a rigorous theory of the number and type of stationary kinetic theory distributions that survive in weak shear flow across the nematic concentration range that encompasses the I-N transi-

tion. Once the shear-onset problem is solved, the continuation problem to finite shear rates is tractable from numerical continuation software, although we shall reveal infinite-period bifurcations beyond current numerical resolution and in need of theoretical guidance. Rigorous kinetic bifurcation theory remains an outstanding challenge.

We substitute the spherical harmonic expansion (Eq. 8) into the Smoluchowski equation (Eq. 1) and project the equation onto the subspace spanned by $\{Y_l^m, m = -l, ...l, l = 0, 2, ..., L\}$. This yields an $[L(L+3)/2]$-dimensional system of ordinary differential equations for $a_{l,m}(t), m = -l, \cdots, l, l = 0, \cdots, L$. Our numerical studies show robust results if $L = 10$, corresponding to a 65-dimensional dynamical system, which we check in random parameter regimes with larger L. We refer to Forest et al. (2002b) for details about the form of the ODE system for $a_{l,m}(t)$, and symmetry properties of Eqs. (1), (2), (3), (4), (5), and (6) with imposed shear. We recall relevant results:

– The Smoluchowski equation, Eqs. (1), (2), (3), (4), (5), and (6), admits an *invariant subspace of in-plane orientation distributions* f, $a_{l,m} = 0$ for all m odd, which generalizes the in-plane mesoscopic tensor criterion $Q_{xz} = Q_{yz} = 0$. Note that our "in-plane" space of PDFs is more general than previous authors, e.g., Maffettone and Crescitelli (1995), which posit $\mathbf{m} = (\cos\theta, -\sin\theta, 0)$. Our definition preserves the quiescent I-N diagram (Fig. 1).

This fact is exploited here to *detect out-of-plane solutions and to detect out-of-plane instabilities of in-plane stable solutions*. (Both features are immediately seen from a comparison of Figs 2 and 3).

– All *out-of-plane solutions* f of Eqs. (1), (2), (3), (4), (5), and (6) have major director which *remains out-of-plane*, and cannot reach the shearing plane except in infinite time. Each such out-of-plane orbit f has a *mirror-symmetric orbit* $\hat{f}$ whose major director is tilted to the other side of the shearing plane.

f and $\hat{f}$ are explicitly related by the transformation $\hat{a}_{l,m} = (-1)^m a_{l,m}$, which affords a strong benchmark on the numerical bifurcation software. Many out-of-plane solution pairs are determined below; when stable, they automatically instill *bistability*. Explicit examples include the out-of-plane steady states labeled **OS**, and periodic solutions we call "tilted kayaking" or "out-of-plane wagging" labeled $\mathbf{K}_2$, which were identified in kinetic simulations by Faraoni et al. (1999), who further recognized their mirror-symmetry. These $\mathbf{K}_2$ orbits have major director which oscillates around an axis that lies strictly between the vorticity axis and shear plane.

– The logrolling steady states (**LR**) and classical kayaking orbits ($\mathbf{K}_1$) of Larson and Ottinger, whose major director aligns with and rotates around the vorticity axis, respectively, are mapped to themselves under reflection through the shear plane. Along with all in-plane distributions, **LR** and $\mathbf{K}_1$ solutions arise in single isolated branches.

These kinetic theory symmetries assert global constraints on the space of solutions for Eqs. (1), (2), (3),

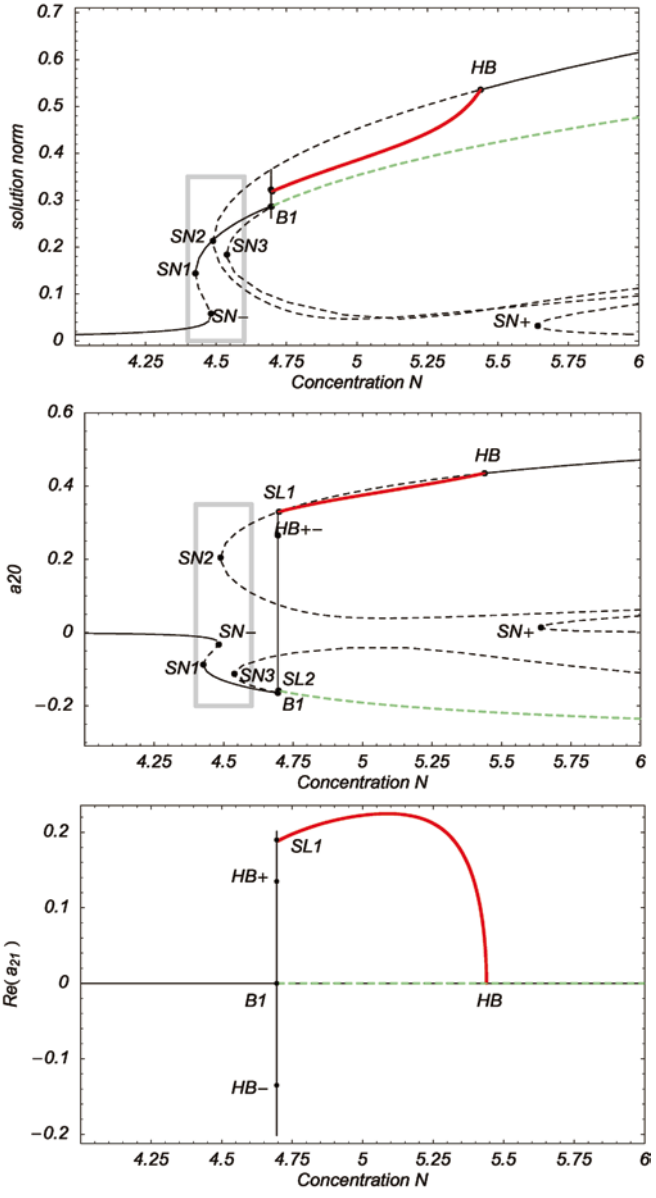

Fig. 2 The bifurcation diagram of all stable and unstable orientational distribution functions f for variable concentration N and fixed weak shear $Pe = 0.1$. *Solid black lines* correspond to stable steady solutions described in detail in the text; *dashed black lines* are unstable steady solutions; the *solid red line* represents stable periodic, out-of-plane kayaking solutions; and the *dashed green line* corresponds to unstable periodic, in-plane tumbling and wagging solutions. The solution norm is the usual 2-norm of the vector $\{a_l^m\}$

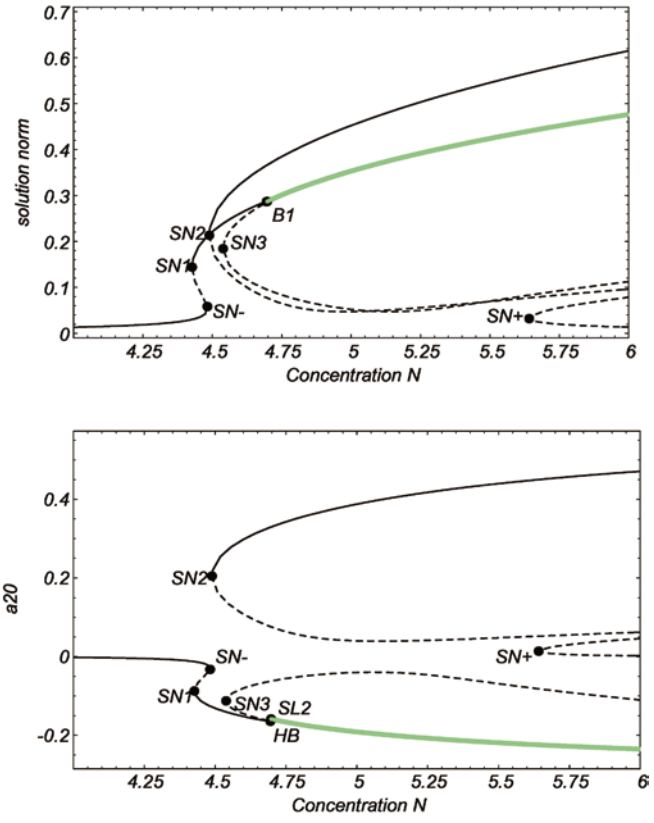

Fig. 3 *In-plane bifurcation diagram* of all stable and unstable orientational distribution functions f for variable concentration N and fixed weak shear $Pe = 0.1$. *Solid black lines* correspond to stable steady solutions, *dashed black lines* are unstable steady solutions; the *solid green line* represents periodic tumbling and wagging solutions that are stable in the restricted in-plane subspace. Comparison with Fig. 2 exposes which in-plane distributions are stable in the restricted subspace yet unstable to out-of-plane perturbations: the top **LR** branch between SL_1 and HB of Fig. 2, and the entire **T**/**W** branch. These results are captured by the Doi closure with finite aspect ratio (Forest et al. 2003a)

(4), (5), and (6); these properties are inherited by moment-closures (Forest et al. 2002b; Forest and Wang 2003). We progress now to a finer resolution of the attractors and unstable states that survive in weak shear, and the relationship between kinetic theory and tensor approximations. Mesoscopic analysis and simulations (Forest and Wang 2003; Forest et al. 2003a) *predict* explicit counts of the multiplicity and stability of monodomain solution branches vs nematic concentration N and normalized shear rate Pe, for Doi-type tensor models; similar methods (Rienacker and Hess 1999; Maffettone et al. 2000) infer in-plane transitions vs shear rate for Hess-type tensor models. These methods apply to any tensor model and allow one to delineate shear-selection criteria that are robust vs sensitive to closure approximation, and to determine model-specific phase transitions as one varies molecular aspect ratio, nematic concentration, or shear rate. One can think of second-moment tensor models as a five-dimensional approximation of kinetic theory that serves as a "predictor". The "mesoscopic predictor" is followed by kinetic theory simulations guided by the above symmetry properties, from which we confirm the robust features and "correct" the sensitive features.

Because of the orientational degeneracy inherent in the mean-field intermolecular potential, the truncation of the infinite-dimensional Smoluchowski equation (Eq. 1) onto a five-dimensional, mesoscopic tensor dynamical system is too crude of an approximation across the range of nematic concentrations that encompass the quiescent isotropic-nematic transition and the onset of weak shear. Indeed, one finds that orders of magnitude greater resolution in the spherical harmonic expansions of f are required to get robust numerical simulations (Faraoni et al. 1999; Grosso et al. 2001; Forest et al. 2002b), and thereby remove ambiguities due to the projection onto second-moment tensor systems. It is nonetheless remarkable that specific kinetic theory features associated with restricted regions of parameter space are qualitatively preserved by individual tensor models; the period-doubling route to chaotic dynamics (Grosso et al. 2001) captured by the Doi closure with finite aspect ratio parameter (Forest and Wang 2003) is one notable example. Various features shared (or not) by kinetic theory and closure approximations are reported below.

Kinetic theory results

This section consists of a detailed analysis and computation of the solution space of the Doi kinetic equation, and discussion of the corresponding previous literature on the relevant stable monodomains.

In Forest and Wang (2003) and Forest et al. (2003a), mesoscopic models determine the following *robust features that are confirmed from the Smoluchowski kinetic simulations in Figs*. 2 and 3. As in Fig. 1, we label critical concentrations N_* at which phase transitions (bifurcations) occur, with $*$ chosen consistent with the bifurcation type and number, e.g., N_{sn-} for the specific saddle-node SN_-. We will build up the weak-shear-perturbed pictures by first ascertaining *the fate of the saddle-node* (SN_0) *and double saddle-node* (DSN_0) *bifurcations of quiescent nematics in Fig*. 1. These features will provide the skeleton upon which we then build up the subsequent finer details.

We exploit the "in-plane" PDF subspace, $\left\{Y_l^m, l = 0, 2, 4, ..., -l \leq m \leq l \text{ with } m \text{ even}\right\}$ (Forest et al. 2002b), with or without flow to detect in-plane shear-induced orientational distributions, and their stability in this confined subspace, e.g., Fig. 3 can be compared with Fig. 2 to detect immediately out-of-plane PDFs and out-of-plane instabilities of in-plane PDFs.

All stationary distributions f are steady at the onset of shear ($0 < Pe \ll 1$) if the nematic concentration N is sufficiently close to the quiescent I-N transition interval $(N_{sn}, N_{dsn}) = (4.49, 5)$ of Fig. 1.

This defines a weak-shear "window" (framed in gray in Fig. 2) of concentrations N for each fixed shear rate, $0 < Pe \ll 1$, $O(Pe)$ close to the quiescent I-N bifurcation window, inside of which *the O(3)-degenerate saddle-node* (SN_0) *of Fig.* 1 *for* $Pe = 0$ *persists as three discrete* $SN_{1,2,3}$ *bifurcations*! This numerical result confirms rigorous mesoscopic analysis (Forest et al. 2003a). In Figs. 2 and 3, this "window" is chosen $4.40 < N < 4.60$, which encloses *the 3 saddle-nodes* $SN_{1,2,3}$*, another saddle node* SN_- *which detaches from the* DSN_0 *bifurcation, and exactly seven branches of weak-shear-selected stationary distributions f* emerging from these four *SN*'s. We amplify this structure first.

- The lowest-norm stable branch for $0 < N < N_{sn-}$ in Fig. 2a is the unique stationary distribution of Eq. (1) for $0 < N < N_{sn1}$, arising from the isotropic branch s_0 of Fig. 1. Mesoscopic analysis (Forest et al. 2003a) predicts, and the kinetic simulation in Fig. 2 confirms: this branch is *in-plane, flow-aligning (***FA***), and stable* until $N = N_{sn-} \approx 4.48$ when it connects to the saddle-node SN_-. Far to the right ($N \geq N_{sn+} \approx 5.64$), the dashed low-norm unstable branch in Fig. 2a is also the continuation of the non-degenerate, unstable isotropic branch of Fig. 1.
- We further depict a_{20} in Fig. 2b, which by Eq. (10) is proportional to the in-plane scalar tensor quantity $Q_{xx} + Q_{yy}$.
- The structurally unstable double saddle-node bifurcation DSN_0 of Fig. 1 "pulls apart" in weak shear, creating two opposing saddle-nodes, SN_- and SN_+ in Fig. 2 and 3.
- The isotropic branch s_0 of Fig. 1 remains isolated and unique, yet fails to persist for $0 < Pe \ll 1$ and concentrations between SN_- and SN_+.

Detailed properties of the stable **FA** branch for $0 < N < N_{sn-}$ are given in Fig. 4. The order-parameter projection of f indicates rather strong biaxiality, even though the degrees of orientation are weak. (All other stable flow-aligned branches at $Pe = 0.1$ are also depicted, and discussed below.) Figure 5 shows the in-plane Leslie-alignment angle computed by projecting f for each N onto the second-moment, then extracting the major director (which is in-plane).

- The other branch emanating from SN_- (and SN_+) in Fig. 2a,b corresponds to one *flow-aligned, unstable state that survives from the continuous O(3) group* s_- *of unstable equilibria from Fig.* 1. *The branch that emerges from* SN_- *turns back for* $N < N_{sn-}$ (and a similar branch turns ahead for $N > N_{sn+}$ out of SN_+).

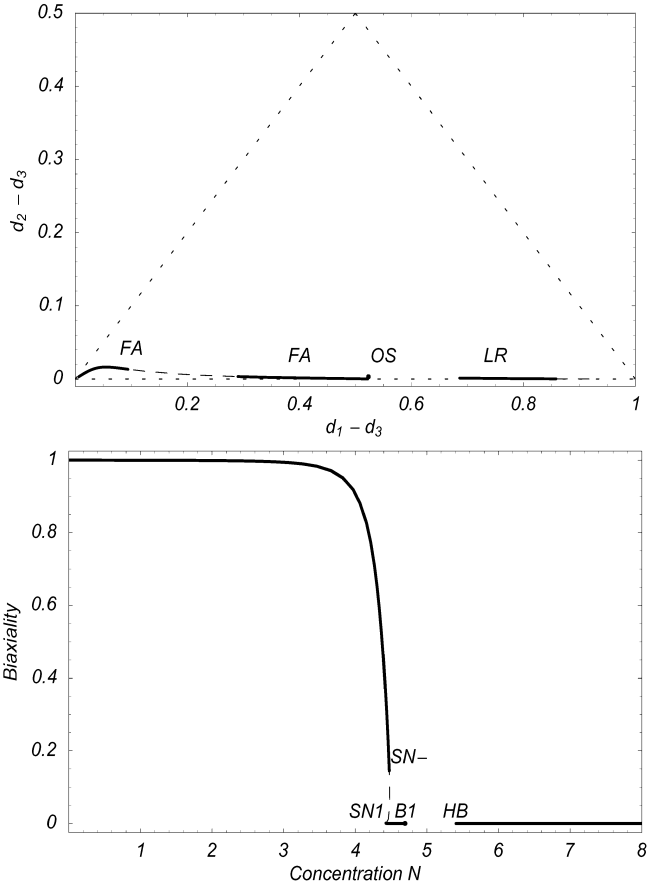

Fig. 4 Order parameter projections and measures of biaxiality for *all stable steady* solution branches of Fig. 2. *Top*: from $\mathbf{Q}(f)$, the order parameters ($d_1 - d_3, d_2 - d_3$) for stable (*solid*) and unstable (*dashed*) solutions along the *"S"*-shaped curve *O-SN–*SN_1*-*B_1 of Fig. 2, and the stable portion past *HB* of the **LR** branch. This diagnostic captures anisotropic order in the respective planes, ($\mathbf{n}_1, \mathbf{n}_2$) of maximum birefringence and ($\mathbf{n}_2, \mathbf{n}_3$) orthogonal to the major director $\mathbf{n}_1$. The *solid black branch* in the *lower-left corner* corresponds to the flow-aligning stable branch *O-SN* $_-$ that emerges from the isotropic solution ($d_1 = d_2 = d_3$). The *dashed black curve* corresponds to the unstable branch *SN–*SN_1, then the *solid black stable* **FA** *branch* corresponds in Fig. 2 to SN_1–B_1. The **OS** branch is resolved as a *large dot* that interpolates the **FA** and unstable logrolling branch of Fig. 2. *Bottom*: the biaxiality parameter (Maffettone et al. 2000), $b = \sqrt{1 - 6Tr\left(\frac{2Q}{Tr(Q^2)}\right)^3}$, is depicted for each *stable* steady branch of Fig. 2. This "degree of biaxiality" complements the birefringence projections (a) to assess whether the mesoscopic orientation $\mathbf{Q}(f)$ is close to uniaxial ($b = 0$) or maximally biaxial ($b = 1$)

One branch connects SN_- to SN_1 in Fig. 2a,b, inside the "window" of N; the other branch continues for $N > N_{sn+}$. Both branches are necessarily unstable at least locally for $0 < Pe \ll 1$ and for N nearby the $SN_\pm$ bifurcations by continuity of linearized eigenvalues with respect to Pe. These branches therefore inherit the instability of s_- as well as possible additional instabilities

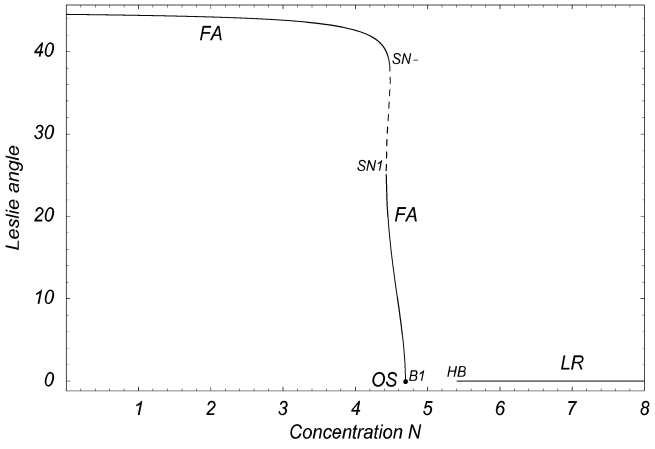

Fig. 5 The Leslie in-plane, flow-alignment angle for steady stable (*solid curves*) solutions vs nematic concentration N at $Pe = 0.1$. The angle for the unstable steady flow-aligning solution is also shown. The gap in steady solutions between B_1 and HB is the regime of unsteady attractors, amplified below (Figs. 9, 11, 12, 13, and 14)

arising from breaking the two zero eigenvalues associated with orientational degeneracy.

This accounts for four steady branches that emerge from the DSN_0 bifurcation of the quiescent I-N diagram of Fig. 1; two branches (O-SN_-, SN_--SN_1) lie inside the "window" defined above, the other two (dashed curves connected to SN_+) lie outside the "indow". All four of these branches are *flow-aligning*, and since they emerge from the DSN_0 bifurcation of Fig. 1, they are nearly isotropic. Only the solid lower branch of Fig. 2a for $0 < N < N_{sn-}$ is stable. Figure 4 measures the degree of anisotropic order in this and other steady stable branches.

– In Fig. 2a,b, *the three distinguished saddle-nodes* $SN_{1,2,3}$ *are the only SN's that survive from the entire* $O(3)$ *group of quiescent* SN_0 *bifurcations of Fig.* 1.

Two are flow-aligning (SN_1,SN_3) orientational distributions, whereas SN_2 corresponds to a logrolling distribution; the two branches emerging from each of $SN_{1,2,3}$ are also in-plane or logrolling. (Otherwise they would have to undergo an instability transition to tip out-of-plane, which does not occur!) This detailed structure of multiplicity and of in-plane and vorticity alignment, can be proven rigorously for algebraic closures in the weak shear limit (Forest et al. 2003a).

By continuity of linearization, once we determine the *multiplicity 3 of SNs surviving the quiescent saddle-node* SN_0, we know that *locally* for $N > N_{sn_j} = 1, 2, 3$, there are two branches coming out of each saddle-node, one corresponding to s_+ (the higher norm branch), the other to s_- . Equivalently, a total of 6 (six) branches of stationary equilibria are shear-selected nearby the three saddle-nodes $SN_{1,2,3}$, *four* of them *are flow-aligning*, and *two are logrolling*.

From each $SN_{1,2,3}$, only one branch can be stable since the other necessarily has at least a one-dimensional instability.

In Figs. 2 and 3, only the three "upper" branches associated with s_+, emanating from $SN_{1,2,3}$, are possibly stable. The delicate question is: **which of these three orientational distributions is stabilized**?

Recall from Forest and Wang (2003), the multiplicity analysis is robust to closure, and from Forest et al. (2003a), for algebraic closures three saddle-nodes persist and they must all be "in-plane" (flow-aligning or logrolling). However, *stability of* **FA** *vs* **LR** *solution branches is closure-sensitive*. Our kinetic simulations determine:

– *For N close to the shear-selected saddle-nodes* $SN_{1,2,3}$, *the kinetic theory stabilizes a unique* **FA** *branch*, shown as the solid branch in Fig. 2a,b connecting SN_1 and B_1. As shown in Fig. 5, this leads to a narrow band of concentrations, $N_{sn1} < N < N_{sn-}$, with *bi-stable FA branches*; this represents preservation of the bi-stable concentration range of quiescent nematics, $N_{sn} < N < N_{dsn}$, Fig. 1.

We further depict in Fig. 2c the out-of-plane component, $Re(a_{21})$, which by Eq. (10) is proportional to Q_{xz}, whose non-zero values highlight *out-of-plane* solution branches. This graph conveys by comparison with Fig. 2a,b that all six solution branches emerging from $SN_{1,2,3}$ are in-plane, i.e., *the major director of* $\mathbf{Q}(f)$ *is either aligned in the shearing plane or along the vorticity axis*, confirming mesoscopic rigorous results with the Doi closure model (Forest et al. 2003a).

Comparison of the full Smoluchowski bifurcation diagram of Fig. 3 for $Pe = 0.1$ with that of Fig. 2 for the *in-plane subspace of distributions f* shows *the* **LR** *branch emerging from* SN_2 *is unstable specifically to out-of-plane instabilities*. Any in-plane analysis will be blind to this instability. This *director-tipping instability of the* **LR** *branch is concentration (N)-dependent*: the instability vanishes at higher concentrations beginning at the Hopf bifurcation labeled HB, so that a *stable* **LR** *branch emerges for* $N > N_{hb}$.

From Forest and Wang (2003), the low-concentration logrolling instability is captured by both the Doi and Tsuji and Rey (1997) closure models, but these closures fail to capture the stabilization at higher N, i.e., they do not capture the bifurcation HB. The Hinch and Leal (1976) closures, on the other hand, incorrectly predict stabilization of the **LR** branch nearby SN_2, fail to predict the stable **FA** branch nearby SN_1, yet correctly predict stable **LR** states at higher N.

As we move outside the "window" of Fig. 2a,b, away from the saddle-nodes $SN_{1,2,3,-}$, **the three branches associated with** s_+ **undergo important transitions at bifurcations labeled** B_1, $HB_\pm$, $SL_{1,2}$ **(and** HB **at higher** N**)**. We amplify these phenomena next.

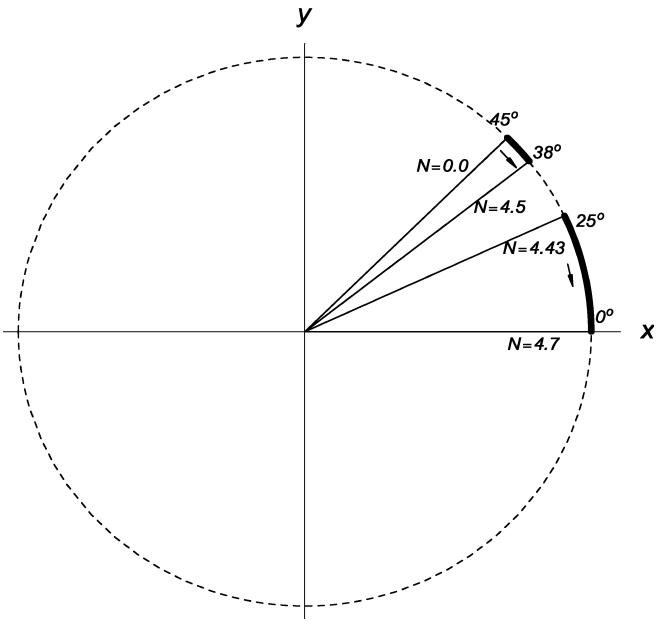

Fig. 6 The change of the Leslie angle for in-plane steady flow-aligning solutions. From Figs. 2 and 3, the *lower solid arc* corresponds to the stable **FA** branch O-SN_- , the *dashed arc* to the unstable **FA** branch SN_--SN_1, then the *top solid arc* to the stable **FA** branch SN_1-B_1

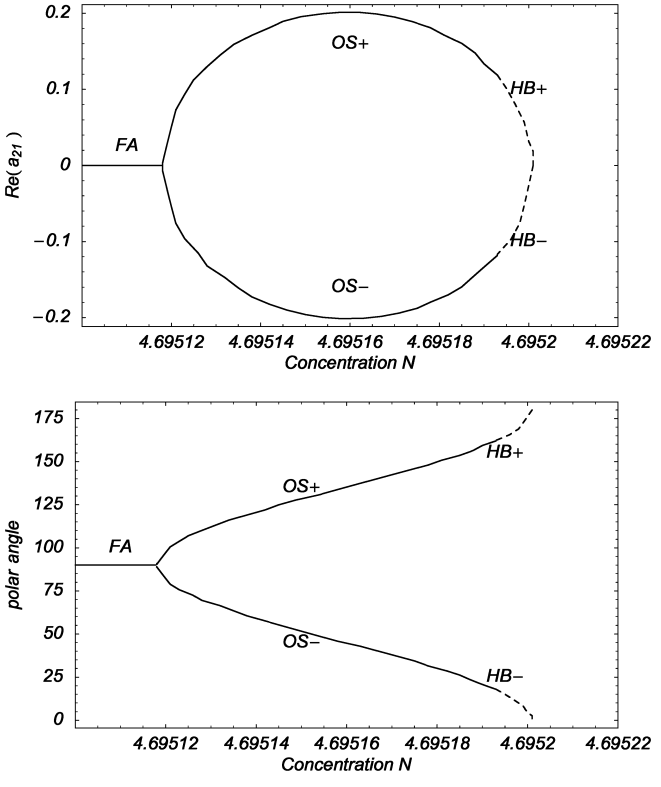

Fig. 7 The out-of-plane steady solutions and their corresponding polar angle θ

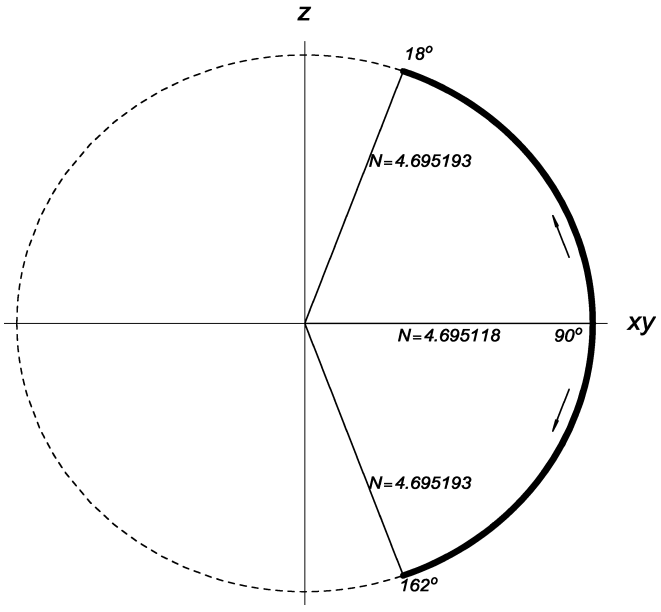

Fig. 8 The polar angle θ of the out-of-plane stable steady solutions $\mathbf{OS}^{+,-}$ for $Pe=0.1$ and $N\in[4.695118,4.695193]$

SL_2 is the onset of the tumbling (**T**) solution with infinite period, marking entry into a band of concentrations (N_{sl2},N_{hb}) where no stable steady distributions exist. This branch of solutions is stable in the in-plane space of distributions as shown in Fig. 3, but *unstable to out-of-plane perturbations* by comparison with Fig. 2. We highlight this result: the **FA** to **T** transition as N varies at weak shear rates is not the stable transition. Instead, as we will see below, the unsteady transition from **FA** results in the kayaking attractor, $\mathbf{K}_1$, elucidated by Larson and Ottinger (1991).

There is a tumbling-wagging (**T-W**) transition on the branch in Figs. 2 and 3 past the bifurcation SL_2, but the entire branch is unstable. Only at higher shear rates does the wagging branch stabilize through a period-doubling bifurcation (see Tables 1 and 2).

Thus *no stable tumbling or wagging states exist, and no stable steady states exist, for the concentration band (N_{sl2},N_{hb}) at $Pe=0.1$.* Note the in-plane Smoluchowski equation, Fig. 3, incorrectly predicts bi-stable tumbling and logrolling stationary states for N between SL_2 and HB (both are unstable), misses the kayaking attractor $\mathbf{K}_1$ altogether, and misses the $\mathbf{K}_1$-**LR** transition at HB.

The Doi and Rey-Tsuji closures both capture the feature of instability of all in-plane (and **LR**) orientational distributions in weak shear inside a band of intermediate concentrations (Forest and Wang 2003), though further details are sensitive to other model parameters.

Since no stable in-plane distributions exist, which out-of-plane orientational distributions emerge as the attracting states at this confluence of bifurcations around B_1 (Figs. 2, 3, and 4)?

Figure 2c is the projection of each solution branch onto the *out-of-plane* component, $Re(a_{2,1})$, which is proportional to the second-moment tensor component, Q_{xz}. There is a nearly vertical, solid, black curve, with two distinguished points labeled $HB_{+,-}$, and a second red curve which persists from this critical concentration N_{SL1} all the way to HB ($N = N_{hb}$) where the solution branch limits to the in-plane logrolling state. *Both of these solution branches are stable, out-of-plane modes*, but of quite different character.

The pitchfork bifurcation at B_1 brings up the "apparently" vertical branch of Fig. 2c, which is blown up in Fig. 7, and corresponds to a *ring of out-of-plane, steady equilibria*, called **OS** by (Faraoni et al. 1999). These branches occur so rapidly in N that the projection in Fig. 2 appears vertical; stability terminates at bifurcations $HB_{+,-}$, Fig. 7. The figures confirm the mirror-symmetry of the Smoluchowski equation (Eq. 1); these states must occur in pairs. For $Pe = 0.1$ as illustrated, the

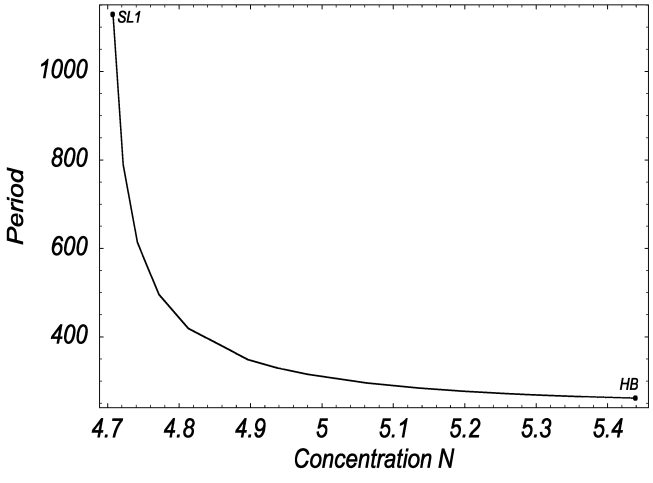

Fig. 9 Periods for the kayaking solutions $\mathbf{K}_1$ for $Pe = 0.1$, between the bifurcation SL_1 and HB of Fig. 2. Note the $\mathbf{K}_1$–**LR** transition, which coincides with the termination of the kayaking branch, occurs at finite non-zero period (a Hopf bifurcation)

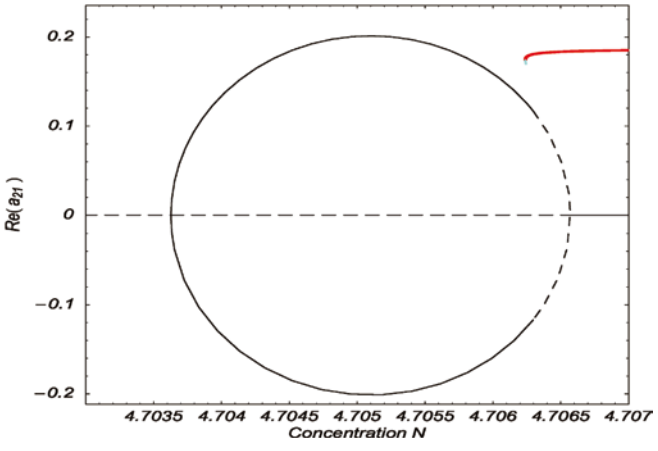

Fig. 10 Co-existence of the stable, steady out-of-plane ($\mathbf{OS}^{+,-}$) pair of solutions (*solid black line*) and the stable kayaking ($\mathbf{K}_1$) solution (*solid red line*) for $Pe = 0.6$. In a very narrow region of (N,Pe), shown in Fig. 15a and Table 1, these states yield tri-stability

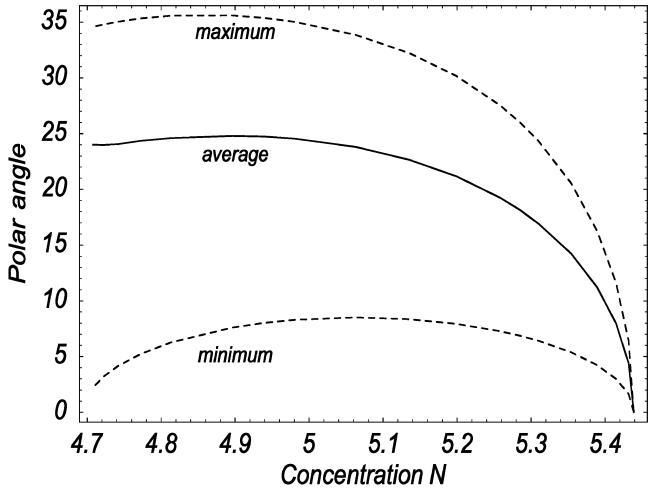

Fig. 11 Maximum and minimum of the polar angle (from the vorticity axis) of the major director of $\mathbf{Q}(f)$ for the stable kayaking branch $\mathbf{K}_1$ (SL_1-HB, Fig. 2), for $Pe = 0.1$. The branch terminates at HB in a **LR** transition through a finite-period Hopf bifurcation. This figure together with Fig. 9, viewed from decreasing N, shows the **LR**–$\mathbf{K}_1$ transition is a classical soft generation of limit cycles (the kayaking orbits), i.e., a second-order phase transition

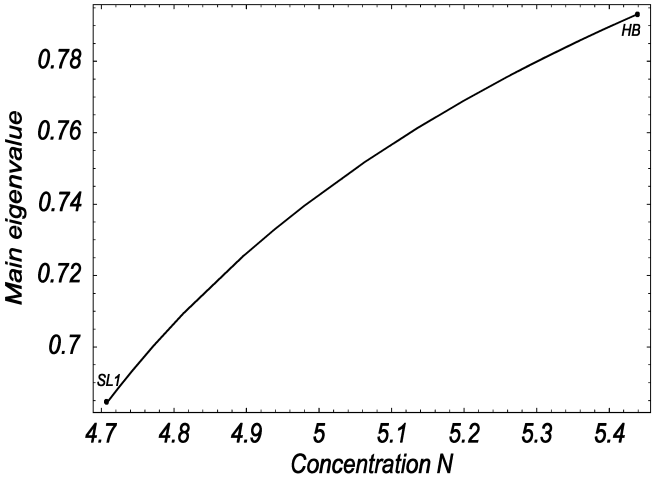

Fig. 12 Maximum eigenvalue d_1 of the second-moment $\mathbf{M}(f)$ for the kayaking branch ($\mathbf{K}_1$) of solutions (SL_1-HB), Fig. 2, $Pe = 0.1$. Each fixed attractor has nearly constant maximum degree of orientation with respect to the major director $\mathbf{n}_1$ of the distribution f. The relative maximum and minimum of $d_1(\mathbf{M}(f))$ over each kayaking orbit differ by less than 0.1%: the $\mathbf{K}_1$ orbits are "director-dominated". Note d_1 increases with N until the **LR** transition at HB when the director locks onto the vorticity axis, after which d_1 continues to increase with N as indicated in Fig. 4a

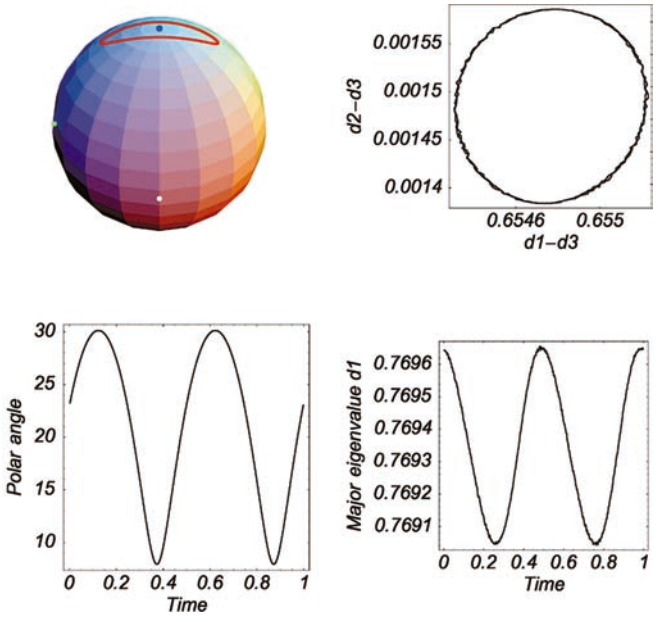

Fig. 13 The Eskimo kayaking solution of Larson & Ottinger corresponding to the $N = 5.2$ orbit of Figs. 11 and 12. The *top left* picture shows the path of the major director on the unit sphere, calculated from $\mathbf{Q}(f(\mathbf{m},t))$. The *blue dot* shows the vorticity (z) axis, the *green dot* shows the flow (x) direction, and the *white dot* marks the flow-gradient (y) direction. The order parameter statistics show two features: $d_2-d_3 \approx 10^{-3}$, which indicates a weakly biaxial second-moment **Q** over the entire orbit; and $d_1-d_3 \approx 0.65$ for all time indicating very little oscillation in the degrees of orientation. The $\mathbf{K}_1$ solutions are "director-dominated" orbits of the PDFf

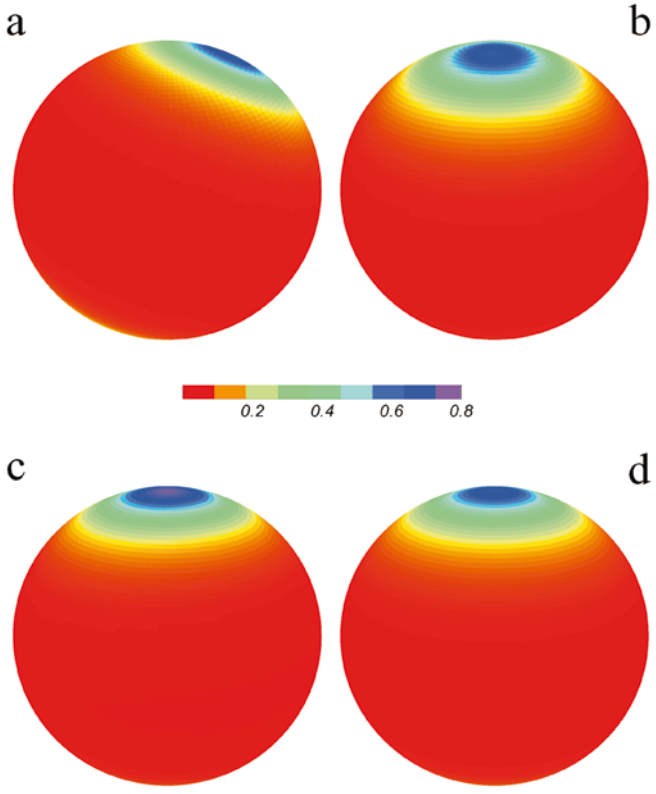

Fig. 14a,b Two snapshots depict $f(\mathbf{m},t)$ along the stable kayaking orbit shown in Fig. 11 for $N = 5.2$ and weak shear rate $Pe = 0.1$; a (respectively b) corresponds to the "pericenter" ("apocenter") where the most probable direction of orientation achieves minimum (maximum) distance to the vorticity axis. **c** Recalls (Forest et al. 2002b) the *quiescent* nematic orientational distribution $f(\mathbf{m})$ of Fig. 1 at $N = 5.2$, where $\boldsymbol{U} \in O(3)$ is chosen so that the distribution is peaked along the vorticity axis. **d** The stable, steady **LR** distribution that emerges at $Pe = 0.1$ at slightly higher concentration (just past the Hopf bifurcation of Fig. 15), $N = 5.45$, which illustrates enhanced focusing of the distribution along the vorticity axis. We note the maximum degree of alignment is $d_1 \approx 0.769$ in a–c, $d_1 \approx 0.7$ in d. (The symmetry $f(\mathbf{m},t) = f(-\mathbf{m},t)$ is hidden by the viewpoint chosen)

OS states exist for an extremely narrow band of concentrations, approximately $4.695118 < N < 4.695193$.

The role of these stable **OS** solution pairs appears to be that of accomplishing a "stiff steady transition" (vs N) from in-plane to out-of-plane alignment, which then undergoes an unsteady transition to kayaking motion $\mathbf{K}_1$ depicted by the solid red curve in Fig. 2. We amplify this mechanism in Figs. 5, 6, 7, and 8.

First we plot the Leslie alignment angle for the in-plane **FA** branch in Figs. 5 and 6; note convergence of the major director to the flow axis as one approaches the termination of the **FA** stable branch. This coincides with onset of the $\mathbf{OS}^{+,-}$ pair, which exists over an exceedingly short range of N. Figures 7 and 8 show the polar angle of the major director of the **OS** solution pair: the polar angle spans from the shearing plane at onset, all the way through approximately 72° to within 18° of the vorticity axis while $\Delta N \approx 10^{-4}$! *During this "stiff" transition in the polar angle, the Leslie angle remains nearly zero*; the major director resides almost in the x-z plane (nearly completely orthogonal to the flow-gradient direction) for all **OS** states! (From the kayaker analogy, the paddle is stationary at a very shallow depth as it "adiabatically" transitions from the flow direction, almost parallel to x-axis, then out-of-plane toward the vorticity axis.)

While these $\mathbf{OS}^{+,-}$ states are structurally unstable from the point of view of bifurcation theory (Chillingworth et al. 2001), they play the role of transitioning from in-plane to out-of-plane stable alignment, followed by an instability of the **OS** states to kayaking motion. *To summarize*, the kinetic equation (Eq. 1) does not yield a first-order phase transition from steady, in-plane **FA** to out-of-plane kayaking motion; *instead, kinetic theory predicts a continuous second-order* **FA** *to* $\mathbf{K}_1$ *transition, mediated by this stiff pair of stable* **OS** *states*. Several mesoscopic models capture these "rings" of **OS** pairs, including the Doi closure (Forest and Wang 2003) and Landau-deGennes model (Chillingworth et al. 2001).

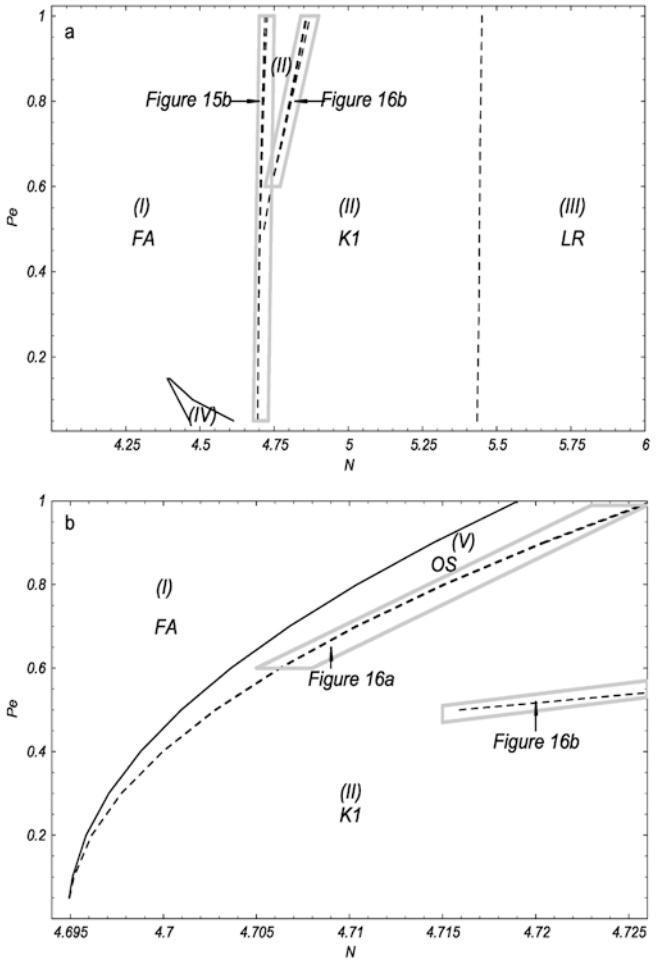

Fig. 15 The concentration-flow (N,Pe) phase diagram of all stable orientational distributions and their transition boundaries. The *top figure* shows Regions I, II, III, and IV comprise the bulk of the diagram. More detailed structure unresolvable on the scale of *the top figure* is placed in *gray frames* and blown-up in the *lower figure*, and then blown-up again in Fig. 16 to resolve further structure. The regions I and III persists for $0 < N < 4$ and $6 < N < 8$, respectively

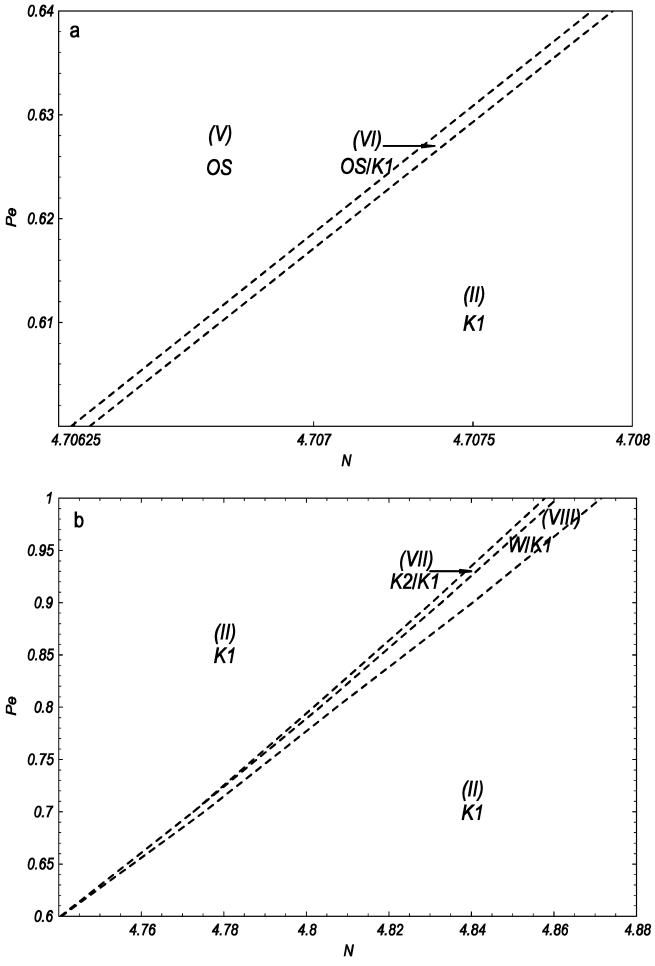

Fig. 16 Blow-up of transition regions and boundaries from Fig. 15. The *top figure* shows a sliver of parameter space in the transition between Regions V and II where the stable out-of-plane steady pair $\mathbf{OS}^{+,-}$ and the kayaking state $\mathbf{K}_1$ co-exist. Note the *vertical scale* is between $Pe = 0.6$ and $Pe = 0.64$, and the *scale in N* is even finer. The detailed structure from the top of Fig. 15 with the small sliver that exists inside of Region II is blown up at the *bottom*. This marks the emergence at weak shear of Region VII where the wagging **W** state emerges, and Region VIII where stable pairs of "tilted kayaking" or "out-of-plane wagging" states $\mathbf{K}_2^{+,-}$ emerge. The boundary between these regions is the $\mathbf{W}$-$\mathbf{K}_2$ transition in which the in-plane periodic wagging mode undergoes an out-of-plane tipping instability, creating the pair of mirror-symmetric, out-of-plane tilted kayaking orbits

At or very close to the termination of the **OS** branch pair, the unsteady transition to a stable "Larson-Ottinger" kayaking solution $\mathbf{K}_1$ occurs.

This is labeled SL_1 in Fig. 2b; the analogous in-plane unsteady tumbling transition is labeled SL_2 in Fig. 2b. Both this $\mathbf{K}_1$ solution and the **OS** pair are absent in the in-plane Smoluchowski equation, Fig. 3. The attractor that emerges is the single kayaking distribution function, whose mirror-symmetric orbit is itself. (We note that the projection onto the shearing plane of the major director $\mathbf{n}_1$ of $\mathbf{K}_1$ could be interpreted as a tumbling orbit experimentally.)

Therefore, **the kayaking orbit $\mathbf{K}_1$ is the unique attractor for concentrations N between the bifurcations SL_1 and HB in the weak flow regime**.

Detailed properties of the kayaking solution branch are given in Figs. 9, 10, 11, 12, 13, and 14. Figure 9 depicts the period of $\mathbf{K}_1$ solutions for $N \in (N_{sl1}, N_{hb})$. The birth at SL_1 of the $\mathbf{K}_1$ branch appears to coincide with an infinite-period Hopf bifurcation which we surmise emerges out of the **OS** "ring" of fixed points shown in Fig. 7. However, we are unable to resolve numerically this structure, and guidance from bifurcation theory will be necessary; e.g., recent work (Chillingworth et al. 2001; Vicente Alonso et al. 2003) identifies the tumbling-wagging transition in terms of a Takens-Bogdanov

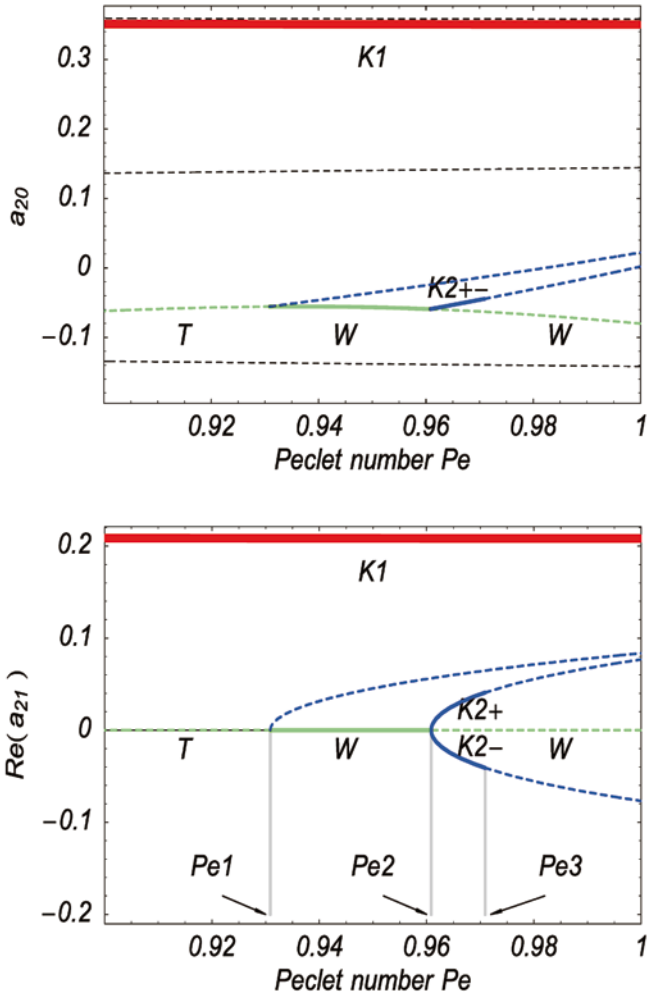

Fig. 17 A vertical slice of Fig. 16b for fixed concentration $N=4.85$ and variable $0.9<Pe<1$. The *solid red stable* $\mathbf{K}_1$ branch exists independently of the three bifurcations labeled $Pe_{1,2,3}$. The unstable **T** (*dashed green*) to stable **W** (*solid green*) transition coincides with onset of an unstable, out-of-plane kayaking pair $\mathbf{K}_2^{+,-}$ (*dashed blue*), which together comprise a periodic pitchfork bifurcation (ppb). Another ppb occurs at Pe_2, where the **W** branch becomes unstable, spawning a stable pair of $\mathbf{K}_2^{+,-}$ (*solid blue*). Finally, at Pe_3, both $\mathbf{K}_2^{+}$ and $\mathbf{K}_2^{-}$ undergo ppb creating *four* stable $\mathbf{K}_2$ branches (not shown). This marks the onset of a rapid sequence of period-doubling bifurcations discovered by Grosso et al. (2001)

bifurcation that extends the previous understanding from Farhoudi and Rey (1993). Figure 9 further shows the rapid decrease in period of the $\mathbf{K}_1$ branch to a finite period at *HB* where the $\mathbf{K}_1$-**LR** transition occurs through a Hopf bifurcation.

Figure 10 is a glimpse at slightly higher $Pe=0.6$ where we are able to track the $\mathbf{K}_1$ branch which now overlaps for a narrow concentration band with the $\mathbf{OS}^{+,-}$ stable pair. $HB_{\pm}$ are infinite-period Hopf bifurcations as indicated by the software AUTO. We suspect there is some organizing structure that connects $HB_{\pm}$ with $\mathbf{K}_1$. This mechanism for the genesis of $\mathbf{K}_1$ orbits is not duplicated thus far by mesoscopic closure models to our knowledge.

Figure 11 illustrates the amplitudes of oscillation of the major director as computed for each kayaking distribution $f(\mathbf{m},t)$. This is calculated by projection onto $\mathbf{Q}(f(\mathbf{m},t))$, followed by determination of the largest eigenvalue d_1 of $\mathbf{M}=\mathbf{Q}+\mathbf{I}/3$, whose eigenvector $\mathbf{n}_1$ is the major director. We then extract the maximum and minimum polar angle (with the vorticity axis) of $\mathbf{n}_1(f(\mathbf{m},t))$ over the kayaking period. The graphs clearly show a convergence as N increases from N_{sl1} to N_{hb}, beginning with large excursions away from the vorticity axis which close down onto the steady vorticity alignment of the **LR** branch.

Figure 12 shows the maximum degree of orientation, d_1, is nearly constant for each kayaking orbit $\mathbf{K}_1$. This behavior suggests a "director-dominated" orientational dynamics of the attracting distributions $\mathbf{K}_1$. Figure 13 illustrates details of the particular $\mathbf{K}_1$ attractor at $N=5.2$ and $Pe=0.1$. The path of the "peak direction of the distribution $f(\mathbf{m},t)$", as indicated by the major director $\mathbf{n}_1(f(\mathbf{m},t))$, shows the classical Eskimo paddle oscillation imagined by Larson and Ottinger. Note the large polar angle excursions yet with the major director staying close to the *x*-*z* plane; i.e., *the paddle stays at a shallow depth and never penetrates deep into the flow gradient direction*, similar to the steady $\mathbf{OS}^{+,-}$ states. Figure 13b shows nearly constant birefringence in all planar cross-sections. Since $\mathbf{n}_1$ oscillates about the vorticity axis, d_1-d_3 is the *maximum birefringence*, which is *greater than the* corresponding *quiescent maximum birefringence* $d_1-d_2=d_1-d_3=0.654$ for $N=5.2$. Note also that $d_2-d_3\approx 10^{-3}$, implying *nearly uniaxial distributions* $f(\mathbf{m},t)$ *throughout the orbit at this low shear rate*.

Figure 14 illustrates two snapshots of the distribution function $f(\mathbf{m},t)$ at the "apocenter" and "pericenter" of the $\mathbf{K}_1$ orbit for $N=5.2, Pe=0.1$. The vorticity-aligned quiescent nematic PDF for $N=5.2$, $Pe=0.0$ (Fig. 14c) and the steady vorticity-aligned **LR** attractor for $N=5.45$, $Pe=0.1$ (Fig. 14d) are shown for comparison.

Continuation of the shear-selection mechanisms to finite shear rates, $0<Pe<1$

Finally, we are in position to summarize the multiplicity, stability, and steady vs unsteady properties of all stationary distributions of the Smoluchowski equation (Eq. 1) for weak shear. The above figures and discussion give details for $Pe=0.1$ and variable N, which we now continue for one more order of magnitude, $0.1\le Pe\le 1$, in Figs. 15 and 16. These figures constitute the *weak shear, flow-phase diagram of large aspect ratio nematic polymers*, indicating *eight distinct regions* in (N,Pe) where a fixed, finite set of stable

solutions exist. We label these Regions I–VIII; Table 1 summarizes the attractor types and total multiplicity for each region.

Regions I (low concentrations), II (intermediate concentrations), and III (high concentrations) consume the majority of the parameter space $0 \le N \le 8$, $0.1 \le Pe \le 1$. Each has a unique attractor: in-plane steady **FA** states in Region I; out-of-plane periodic $\mathbf{K}_1$ states in Region II; and steady **LR** states in Region III.

The small "fin" Region IV for low *Pe* has *bi-stable* **FA** steady states. This is the weak-shear continuation of the quiescent concentration band $N_{sn} < N < N_{dsn}$, Fig. 1, where the isotropic (s_0) and nematic (s_+) steady states are bi-stable. The steady structure of Region IV inside of Region I also occurs in steady extensional flow (Forest et al. 2000, 2001).

Region V has bi-stable, out-of-*plane, steady states* labeled $\mathbf{OS}^{+,-}$. These states have been described in Figs. 6, 7, 8, and 10. Region V is the thin transition region between Region I and II, blown-up in Figs. 15b and 16a.

Region VI is an even thinner region between V and II where stable kayaking $\mathbf{K}_1$ and bi-stable $\mathbf{OS}^{+,-}$ states co-exist, shown in Fig. 16a.

Regions VII and VIII contain bi-stable "tilted kayaking" orbits $\left(\mathbf{K}_2^{+,-}\right)$, respectively wagging (**W**) attractors, which co-exist with the stable kayaking branch $\mathbf{K}_1$. These regions are only resolvable numerically for $Pe \gtrsim 0.5$, Fig. 15b, and blown up in Fig. 16b.

The boundaries between these Regions of fixed attractors are summarized in Table 2. These correspond *physically* to various phase transitions, *mathematically* to specific bifurcation structures.

Table 2 provides some insights into the transition phenomena and corresponding states that are responsible for the bifurcations between Regions. A few of these structures are straightforward "textbook" bifurcations:

- The saddle-nodes bounding regions IV and I
- The $\mathbf{K}_1$-**LR** transition between II and III is a finite-period Hopf bifurcation
- The steady, in-plane to out-of-plane transition from **FA** to $\mathbf{OS}^{+,-}$ between regions I and V is a classical pitchfork bifurcation

Yet other bifurcations are natural to large-dimensional dynamical systems. In Fig. 17 we fix $N = 4.85$ and blow-up the vertical slice of Fig. 16b for $0.9 \le Pe \le 1.0$ to amplify three more of the bifurcation boundaries at concentrations labeled $Pe_{1,2,3}$, all of which occur in the presence of the kayaking attractor $\mathbf{K}_1$:

- Pe_1: The unstable **T** (tumbling) to stable **W** (wagging) transition between regions II and VIII coincides with the emergence of an unstable $\mathbf{K}_1$, which constitutes a pitchfork bifurcation of periodic solution branches.
- Pe_2: Another periodic pitchfork bifurcation defines the transition regions VIII and VII where the stable **W** branch forks into an unstable **W** and a pair of stable $\mathbf{K}_2^{+,-}$ orbits.
- Pe_3: The first of a cascade of period-doubling bifurcations of the $\mathbf{K}_2^{+,-}$ attractors, which require further blow-up. This region marks entrance into the chaotic regime discovered by Grosso et al. (2001), the details of which are beyond this paper. Remarkably, this period-doubling route to chaotic dynamics is captured

Table 1 Regions in (N,Pe) with type and number of PDF attractors. The Regions are defined in Figs. 15 and 16. The subscripts i and n for **FA** states indicate their origin at $Pe = 0$ from isotropic (i) or nematic (n) equilibria

Region	Attractor type	Attractor multiplicity
I	**FA**	1
II	$\mathbf{K}_1$	1
III	**LR**	1
IV	$\mathbf{FA}_i$, $\mathbf{FA}_n$	2
V	$\mathbf{OS}^+$, $\mathbf{OS}^-$	2
VI	$\mathbf{OS}^+$, $\mathbf{OS}^-$, $\mathbf{K}_1$	3
VII	$\mathbf{K}_1$, $\mathbf{K}_2^+$,$\mathbf{K}_2^-$	3
VIII	**W**, $\mathbf{K}_1$	2

Table 2 Attractor transitions for nematic polymers in weak shear $0 < Pe \le 1$, and for the dilute to concentrated range $0 < N < 8$. The regions are defined in Figs. 15 and 16 and the fixed attractors in each region are listed in Table 1

Boundary (left to right)	Bifurcation type	Attractor transition (left to right regions)
I–II	Saddle node	Inique to bi-stable **FA**
II–I	Saddle node	Bi-stable to unique **FA**
I–V	Steady pitchfork	Steady in-plane **FA** to out-of-plane $\mathbf{OS}^{+,-}$ transition
V–VI	Saddle-loop	Onset of $\mathbf{K}_1$ attractor
VI–II	∞-Period, unstable Hopf	Stable to unstable transition of $\mathbf{OS}^{+,-}$
II–VII	Complex period-doubling cascade (requires further blow-up)	Emergence of out-of-plane, periodic, bi-stable $\mathbf{K}_2^{+,-}$
VII–VIII	Periodic pitchfork	Unstable to stable transition of **W** and stable to unstable transition of $\mathbf{K}_2^{+,-}$
VIII–II	Period-doubling	Stable**W** to unstable**T** transition and loss of unstable $\mathbf{K}_1$
II–III	Supercritical,finite-period Hopf	Periodic$\mathbf{K}_1$ to steady **LR** transition

by the Doi closure with finite aspect-ratio molecules (Forest and Wang 2003).

The bifurcation between regions V and VI requires further clarification both theoretically and numerically.

Rheological features of the weak-shear phase diagram

The formulas for computing the first and second normal stress differences N_1 and N_2, and the shear stress η are listed in the appendix. Our purpose now is to evaluate these rheological features across the weak shear phase diagram, from which experimental data on nematic polymers (cf. Larson 1999) can be correlated. We begin by taking two cross sections of the phase diagram, Figs. 15 and 16, first fixing $Pe = 0.1$, and then fixing $N = 4.85$.

From Fig. 15, the horizontal slice $Pe = 0.1$ gives the *concentration-dependent states and phase transitions in slow flow* shown in Table 3.

In Fig. 18, we graph N_1, N_2, and η for the in-plane steady flow-aligning states $\mathbf{FA}_i$, $\mathbf{FA}_n$ vs $0 < N < 4.6951$.

For the *perturbed isotropic branch* $\mathbf{FA}_i$: $N_1 > 0$ and $N_2 < 0$ with $|N_1| \sim O(10^{-3})$, $|N_2| \sim O(10^{-5})$. Furthermore, though small, $|N_1|, |N_2|$ increase with N . The shear stress η is nearly constant.

For the *perturbed nematic in-plane steady state* $\mathbf{FA}_n$: $N_1 > 0$ and $N_2 < 0$; both N_1 and N_2 monotonically approach zero as N approaches $N \approx 4.695$, i.e., as the flow-aligning ($\mathbf{FA}_n$) to out-of-plane steady (**OS**) transition occurs. The apparent viscosity η drops in half over this narrow concentration range.

The out-of-plane steady states $\mathbf{OS}^{+,-}$ are not likely to be seen in laboratory experiments. Nonetheless, since they mediate the flow-aligning (**FA**) to kayaking ($\mathbf{K}_1$) transition vs N, we give N_1, N_2, and η for this extremely narrow range of concentrations in Fig. 19.

In the narrow band of $\mathbf{OS}^{+,-}$ steady states, $4.6951 < N < 4.6952$, while numerical values are quite small, *both* N_1 *and* N_2 *change sign*! (We note that these sign changes are *not* an artifact of the low $Pe = 0.1$; we have confirmed this behavior of the $\mathbf{OS}^{+,-}$ branch vs N all way to $Pe = 0.8$.)

The $\mathbf{FA}_n$-$\mathbf{OS}^{+,-}$ transition, where in-plane alignment moves out-of-plane, Fig. 7, signals minimum of N_1 and η, and a local maximum of N_2 (compare Figs. 18 and 19).

Table 3 Concentration-dependent stable states and transitions for fixed weak shear rate $Pe = 0.1$

Transition N	4.43		4.48	4.6951	4.6952	5.44
Stable state(s)	FA_i	FA_i/FA_n	FA_n	$\mathbf{OS}^{+,-}$	$\mathbf{K_1}$	**LR**

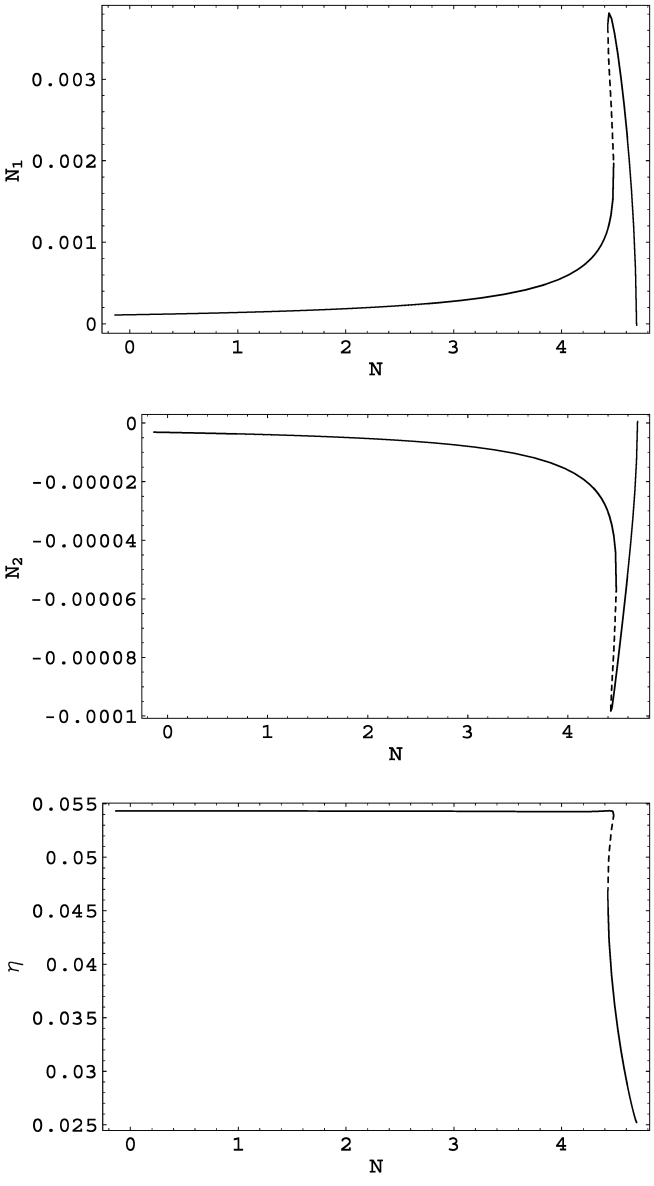

Fig. 18 First and second normal stress differences N_1 and N_2, and the shear stress for the flow-aligning solutions. The weak normalized shear rate is $Pe = 0.1$

As the $\mathbf{OS}^{+,-}$ first go unstable then disappear, the kayaking stable branch ($\mathbf{K}_1$) emerges, Fig. 10, and persists as a stable periodic response until the **LR** transition at higher $N \approx 5.44$.

The $\mathbf{K}_1$ orbit is a primary attractor for intermediate concentrations in weak shear; at $Pe = 0.1$, $\mathbf{K}_1$ is stable for $4.6952 < N < 5.44$. A small parameter region of stable periodic solutions, $\mathbf{W}$ or $\mathbf{K}_2^{+,-}$, *coexist* with $\mathbf{K}_1$, which we amplify later.

Figure 20 shows that along the $\mathbf{K}_1$ branch of attractors, $N_1 > 0$ over the full period of a specific $\mathbf{K}_1$ solution, and further that $\langle N_1 \rangle$ decreases toward zero as the **LR** transition is approached at $N = 5.44$.

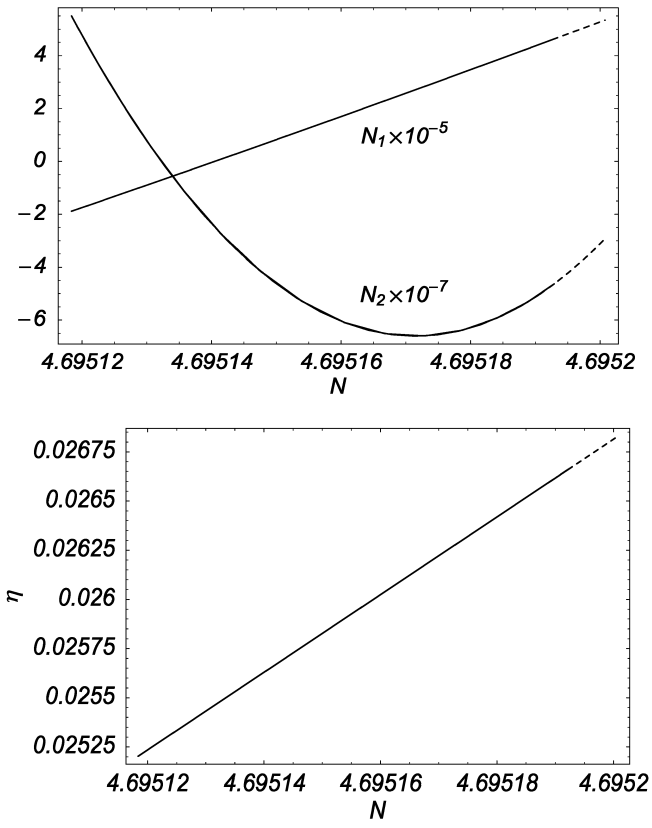

Fig. 19 First and second normal stress differences N_1 and N_2, and the shear stress for out-of-plane solutions at fixed weak shear rate $Pe = 0.1$

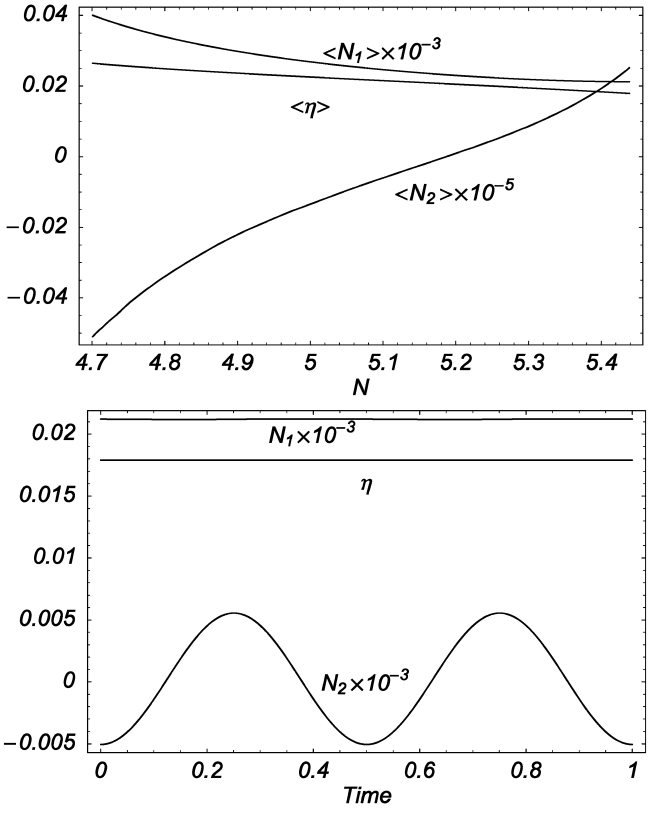

Fig. 20 *Top*: first and second normal stress differences N_1 and N_2, and the shear stress for $\mathbf{K}_1$ solutions. Parameters are $a = 1$, $Pe = 0.1$. *Bottom*: evolutions of first and second normal stress differences N_1 and N_2, and the shear stress for a specific $\mathbf{K}_1$ solution at $N \approx 5.437$

N_2 hovers near zero for all $\mathbf{K}_1$ solutions, indeed oscillating about zero. As Fig. 20 shows, $\langle N_2\rangle \approx O(10^{-7})$, yet changes from negative to positive at $N \approx 5.2$.

Apparent viscosity $\langle\eta\rangle$ decreases for $\mathbf{K}_1$ orbits as N increases, by a factor of about 2/3.

Rheological features for logrolling **LR** states are reported in Fig. 21.

Both N_1 and N_2 are positive for **LR** attractors, yet nearly zero ($N_1 \approx 10^{-5}$, $N_2 \approx 10^{-7}$). N_1 decreases with N, while N_2 is non-monotone.

Apparent viscosity steadily decreases with higher concentration.

Most experiments fix concentration and vary the shear rate. This corresponds to a vertical slice of the bifurcation diagram Fig. 15. To illustrate, we fix $N = 4.85$ (just above the quiescent I-N transition), which fixes the molecular properties of the liquid, and determine the effect of variable shear rate Pe on the shear stress and normal stress differences. The bifurcation diagram between $0 < Pe < 3$ is shown in Fig. 22, with details around $Pe = 0.95$ already shown earlier in Fig. 17. This slice of the phase diagram (Fig. 15) also allows us to highlight the *bi-stable and tri-stable*

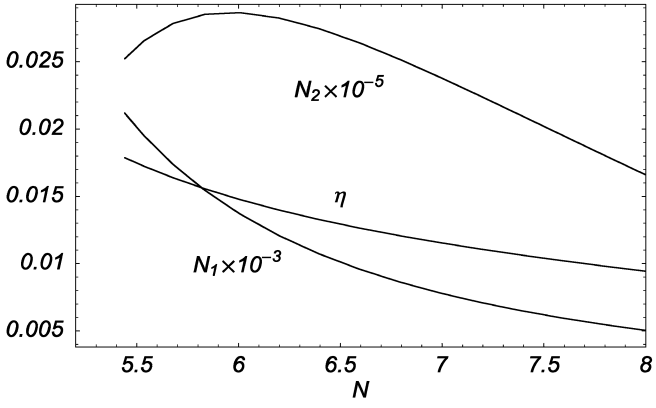

Fig. 21 First and second normal stress differences N_1 and N_2, and the shear stress for the stable logrolling solutions at fixed weak shear rate $Pe = 0.1$, which exist for the concentration $N > N_h = 5.439$

parameter regimes. The results are summarized as follows. Table 4 depicts the attractor number and type over six intervals of shear rate, with transitions at the five indicated rates.

For $\mathbf{K}_1$ solutions, which persists for $0 < Pe < 2.26$, as shown in Fig. 20 and consistent with Fig. 20:

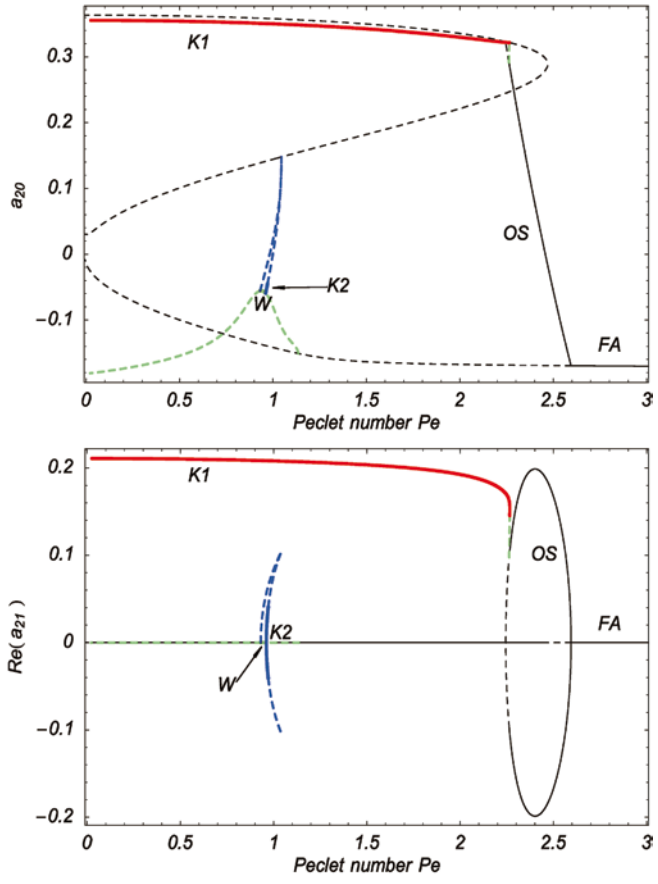

Fig. 22 Bifurcation diagram of all stable and unstable states for variable Peclet number *Pe* and fixed concentration $N = 4.85$. *Solid lines* correspond to stable states, while *dashed lines* corresponds to unstable states. The detail around **W** and $\mathbf{K}_2$ has been shown in Fig. 17. There are yet more complex branches not shown here associated with the transition between the $\mathbf{K}_1$ and **OS** branches

Table 4 *Pe* -dependent stable states and *Pe*-induced transitions for the concentration$N = 4.85$. The indicated values of *Pe* denote transitions in number and/or type of attractors

Transition Pe	0.93	0.96	0.97	2.26	2.59
Stable state(s)	$\mathbf{K_1}$	$\mathbf{K_1}$/W	$\mathbf{K_1}/\mathbf{K_2^{+,-}}$	$\mathbf{K_1}$	$\mathbf{OS}^{+,-}$	**FA**

$\langle N_1 \rangle > 0$ and $\langle N_1 \rangle$ increases with *Pe*, while $\langle N_2 \rangle < 0$ and $\langle N_2 \rangle$ decreases.

For the specific $\mathbf{K}_1$ solution at $Pe = 0.952$, Fig. 23 shows $N_1 > 0$ for the entire periodic orbit while N_2 oscillates around 0.

Although **W** and $\mathbf{K}_2^{+,-}$ coexist with $\mathbf{K}_1$ in a narrow interval, there is no apparent influence on the rheology of $\mathbf{K}_1$. For $0.97 < Pe < 2.26$, $\mathbf{K}_1$ orbits are the unique stable attractors once again. Figure 23 shows $\langle N_1 \rangle$ continues to increase, and $\langle N_2 \rangle$ continues to decrease, while η is nearly constant.

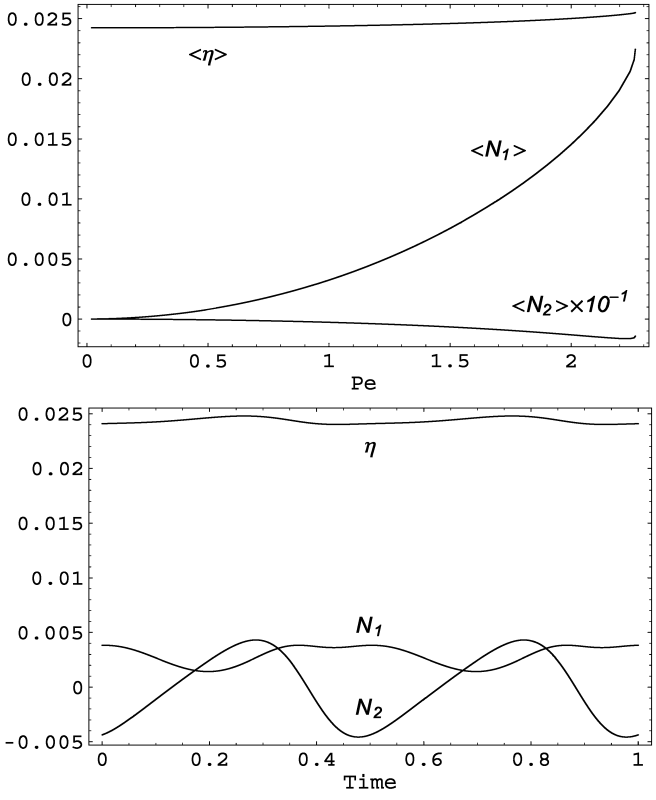

Fig. 23 *Upper*: first and second normal stress differences N_1 and N_2, and the shear stress for the kayaking $\mathbf{K}_1$ solutions. The concentration is $N = 4.85$. *Bottom*: first and second normal stress differences N_1 and N_2, and the shear stress for the specific kayaking $\mathbf{K}_1$ solution at $Pe = 0.952$ in one period

We next analyze the *co-existing stable states*, **W** then $\mathbf{K}_2^{+,-}$, and their comparison with the $\mathbf{K}_1$ rheology. We plot the stress properties for **W** and $\mathbf{K}_2$ solutions together in Fig. 24 to explore their transition at $Pe = 0.96$.

For *both* **W** *and* $\mathbf{K}_2^{+,-}$ *solutions*, $\langle N_1 \rangle < 0, \langle N_2 \rangle > 0$. Note $\langle N_1 \rangle$ has *opposite sign* to that of the co-existing $\mathbf{K}_1$ stable orbits for both **W** and $\mathbf{K}_2^{+,-}$ branches. This implies that two separate experiments of the same nematic polymer at identical flow rates can yield $\langle N_1 \rangle > 0$ *and* $\langle N_1 \rangle < 0$!

The wagging to kayaking (**W**-$\mathbf{K}_2^{+,-}$) transition *coincides with local minima* of N_1 and η, and *local maxima* of N_2, as opposed to sign changes.

Figure 25 shows the behavior in one period of the **W** solution (top) at $Pe = 0.952$ and the $\mathbf{K}_2$ solution (bottom) at $Pe = 0.961$. They are remarkably similar. Note that for specific wagging **W** and kayaking $\mathbf{K}_2$ solutions, N_1 and N_2 oscillate in time through zero, although their averages are negative and positive, respectively.

We also checked normal stress differences and apparent viscosity for several other slices from the phase diagram, Fig. 15. The results are plotted in Fig. 26. From these results, it appears that "Region I" in the flow curve of Onogi and Asada (1980) is not captured by

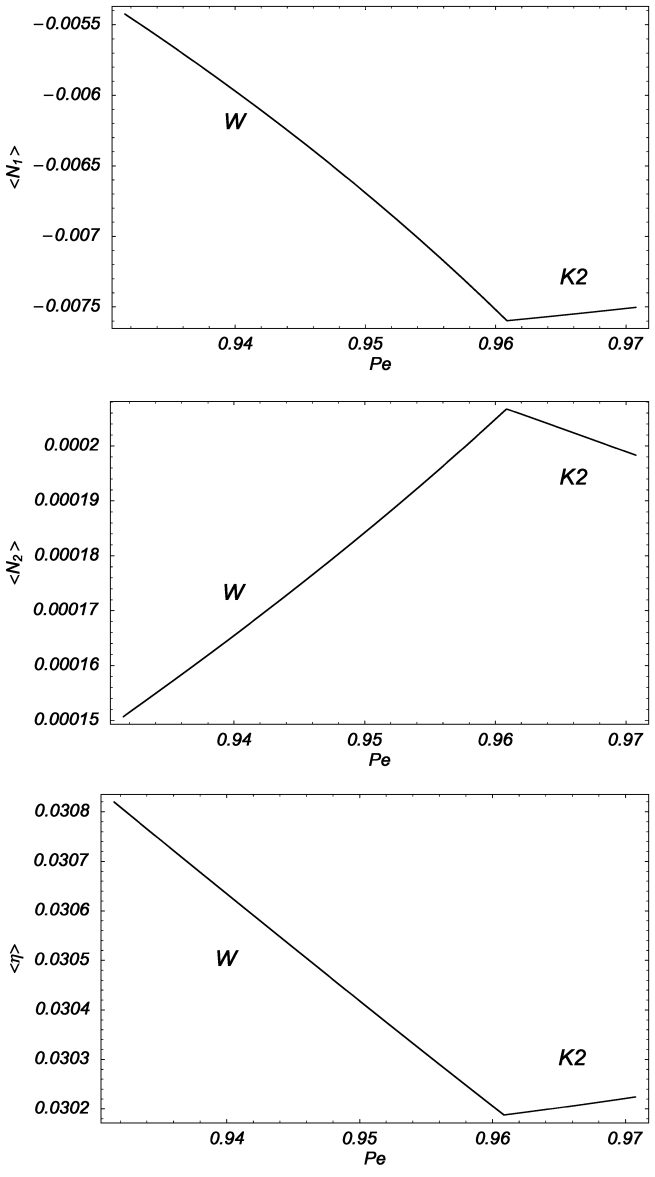

Fig. 24 First and second normal stress differences N_1 and N_2, and the shear stress for the wagging **W** and Kayaking $\mathbf{K}_2$ solutions. The concentration is $N = 4.85$

the Doi theory with constant rotational diffusivity for the concentration range studied here. We recall from Larson (1999), Fig. 11.6, the caption notes "For some LCPs, the low-shear-rate Region I is not found".

As a summary of special features, in the region $0 < Pe < 1$, $0 < N < 8$, we list signs of normal stress differences $\langle N_1 \rangle$, $\langle N_2 \rangle$, averaged over periodic orbits, in Table 5. Note that *in the anomalous weak shear rate regime*, sign changes in $\langle N_1 \rangle$ or $\langle N_2 \rangle$ are more the norm than the exception! This is perhaps to be expected because their magnitudes are so small. The extension of these rheological features to higher shear rates will be reported in a sequel.

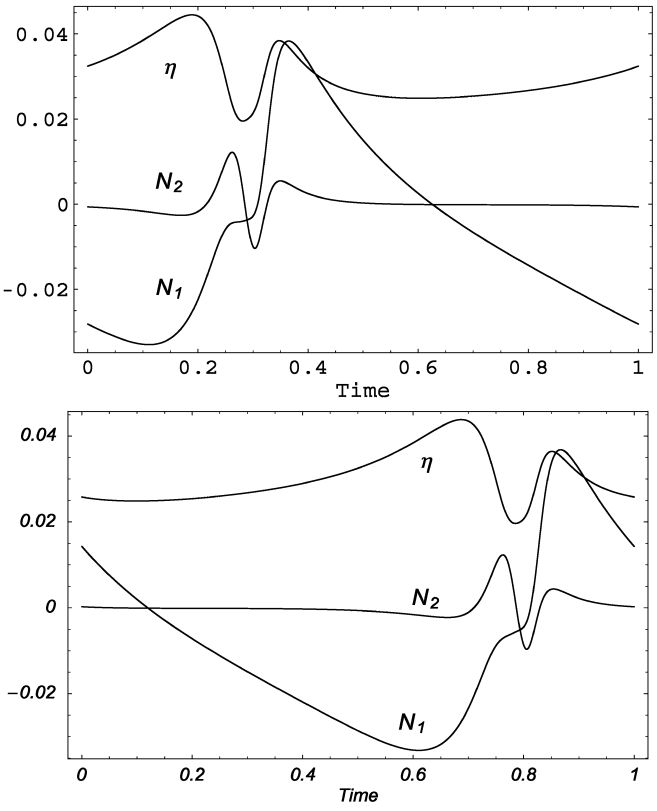

Fig. 25 First and second normal stress differences N_1 and N_2, and the shear stress in one period for specific periodic states. *Top*: wagging **W** solution at $Pe = 0.9507$. *Bottom*: kayaking $\mathbf{K}_2$ solution at $Pe = 0.961$

Table 5 Signs of normal stress differences, $\langle N_1 \rangle$ and $\langle N_2 \rangle$, averaged over periodic orbits, for each monodomain attractor type that occurs for $N > 0$, $0 < Pe < 1$. Regions are defined in Figs. 15 and 16. The $\pm$ sign indicates sign changes occur for those attracting states *within* the parameter region

Region	Attractor type	$< N_1 >$	$< N_2 >$
I	**FA**	+	–
II	$\mathbf{K_1}$	+	$\pm$
III	**LR**	+	+
IV	$\mathbf{FA_{i,n}}$	+	–
V	$\mathbf{OS}^{+,-}$	+	$\pm$
VI	$\mathbf{K_1}$, $\mathbf{OS}^{+,-}$	+,+	$\pm$, $\pm$
VII	$\mathbf{K_1}$, $\mathbf{K_2}^{+,-}$	+,–	$\pm$, +
VIII	$\mathbf{K_1}$, $\mathbf{W}$	+,–	$\pm$, +

Conclusion

The weak-shear monodomain attractors and transition phenomena of Doi kinetic theory have been detailed; these results stand as the benchmark for experimental comparisons. Furthermore, this resolved phase diagram is now poised to guide the continuation into higher shear

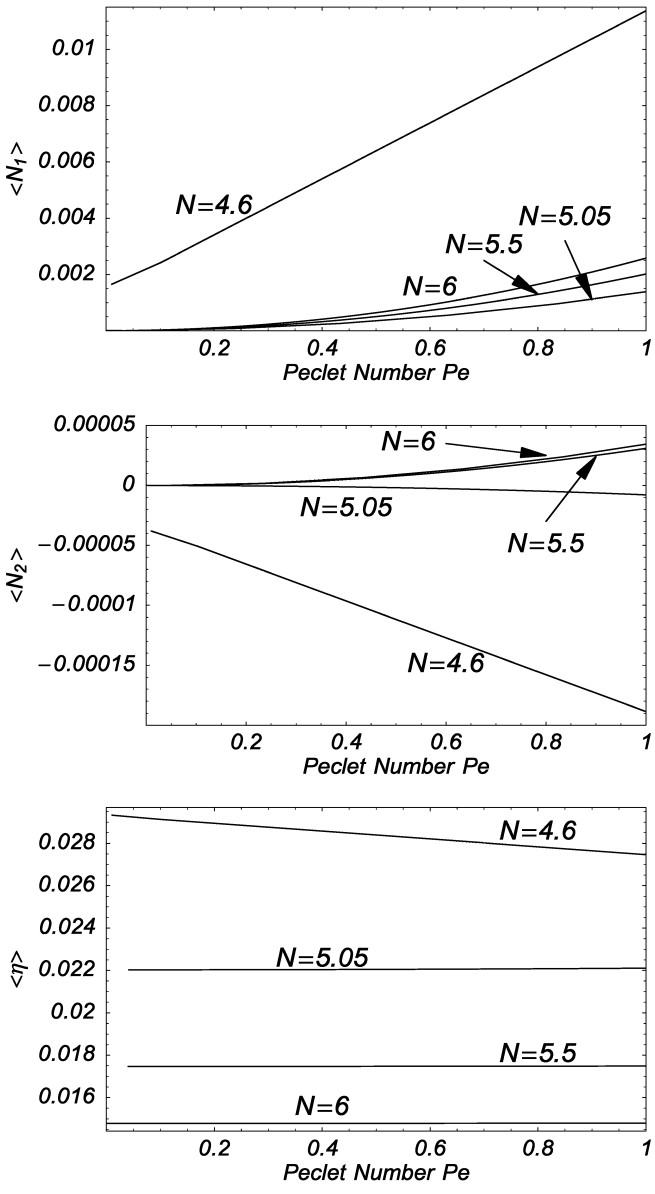

Fig. 26 First and second normal stress differences N_1 and N_2, and the shear stress η for several vertical slices in Fig. 15. The stable state is **FA** for $N = 4.6$, $\mathbf{K}_1$ for $N = 5.05$, and **LR** for $N = 5.5{,}6$

rates (cf. Faraoni et al. 1999; Grosso et al. 2001). A variety of subtle attractor properties of the Doi kinetic theory have been clarified by a combination of mesoscopic predictions and detailed kinetic theory simulations. The issues of multiplicity, in-plane vs out-of-plane, and stability of stationary orientational distributions have been mostly resolved in this study, and the remaining questions have been identified. The general conclusion of this study is that anomalous weak shear behavior is indeed predicted by the Doi kinetic theory. There are, on the other hand, regions of concentration and shear rate with robust monodomain responses, i.e., fixed attractor type and fixed rheological features (signs of N_1, N_2). These regions are denoted I, II, III in Fig. 15 with attractors **FA**(I), $\mathbf{K}_1$(II), **LR**(III). The transition from Region I to II to III is achievable through fixed *Pe*, while varying concentration from the low (I) to intermediate (II) to high (III) range. $\langle N_1 \rangle > 0$ in all three regions, whereas $\langle N_2 \rangle$ is negative in Region I, changes sign in Region II, and is positive in Region III. On the other hand, these transitions are *not simple*, involving other stable monodomain responses which coexist with $\mathbf{K}_1$ in narrow parameter regions, and which have *different rheology* than $\mathbf{K}_1$. The existence of these complex transition regions earns the weak shear phase diagram the title of "anomalous". The extension of the transition regions to higher shear rates will be addressed in a sequel.

These detailed kinetic attractor regimes also serve as benchmarks for closure approximations of kinetic theory for nematic polymers. Clearly, the bifurcation phenomena amplified here will defy any attempt to capture the entire structure with second-moment closures, as we have annotated during the discussions. Specific closures are capable of reproducing quite complex features *if* one restricts to a limited region of (N, Pe) space. With respect to the rich bifurcation structures in weak shear, it is highly unlikely that any a priori second-moment closure rule is capable of capturing the flow-phase diagram of kinetic theory.

Acknowledgment and disclaimer Effort sponsored by the Air Force Office of Scientific Research, Air Force Materials Command, USAF, under grant number F49620-99-1-0003 and F49620-00-1-0008. This work is supported in part by the NASA University Research, Engineering and Technology Institute on Bio Inspired Materials (BIMat) under award No. NCC-1-02037. Partial support is acknowledged from the National Science Foundation through grants NSF0115445, 0072553, 0308019. The US Government is authorized to reproduce and distribute reprints for governmental purposes notwithstanding any copyright notation thereon. The views and conclusions contained herein are those of the authors and should not be interpreted as necessarily representing the official policies or endorsements, either expressed or implied, of the Air Force Office of Scientific Research or the US Government.

Appendix. Stress formulas

The extra stress in dimensional form is given by Wang (2002):

$$\begin{aligned}\tau = {} & (\eta_0 + 3\nu kT\varsigma_3)\mathbf{D} \\ & + 3a\nu kT\left[\mathbf{Q} - N\left(\mathbf{Q} + \frac{\mathbf{I}}{3}\right)\mathbf{Q} + N\mathbf{Q} : \langle \mathbf{mmmm} \rangle\right] \\ & + 3\nu kT[\varsigma_1(\mathbf{DM} + \mathbf{MD}) + \varsigma_2 \mathbf{D} : \mathbf{M}_4]\end{aligned} \tag{A1}$$

where η_0 is the isotropic viscosity, ς_0 is a free parameter determined experimentally, v is the molecule number density, and all other parameters are prescribed by the molecule aspect ratio r:

$$\varsigma_3 = \frac{\varsigma^{(0)}}{I_1}, \quad \varsigma_1 = \varsigma^{(0)}\left(\frac{\mathrm{I}}{I_3} - \frac{\mathrm{I}}{I_1}\right), \quad \varsigma_2 = \varsigma^{(0)}\left[\frac{J_1}{I_1 J_3} + \frac{\mathrm{I}}{I_1} - \frac{2}{I_3}\right],$$

$$I_1 = 2r\int_0^\infty \frac{dx}{\sqrt{(r^2+x)}(1+x)^3},$$

$$I_3 = r(r^2+1)\int_0^\infty \frac{dx}{\sqrt{(r^2+x)}(1+x)^2(r^2+x)},$$

$$J_1 = r\int_0^\infty \frac{xdx}{\sqrt{(r^2+x)}(1+x)^3},$$

$$J_3 = r\int_0^\infty \frac{xdx}{\sqrt{(r^2+x)}(1+x)^2(r^2+x)}, \qquad \text{(A2)}$$

In our calculations, we have used values $\varsigma_1 = 0$, $\varsigma_2 = 0.1$, $\varsigma_3 = 0.001$, consistent with extremely large aspect ratio rod-like nematic polymers, $r \gg 1$. The first and second normal stress differences N_1 and N_2, and the shear stress η are computed as

$$\begin{aligned} N_1 &= \tau_{xx} - \tau_{yy}, \\ N_2 &= \tau_{yy} - \tau_{zz}, \\ \eta &= \tau_{xy}/Pe. \end{aligned} \qquad \text{(A3)}$$

We normalize stress by $3v$ kT in all figures.

References

Advani SG, Tucker CL (1987) The use of tensors to describe and predict fiber orientation in short fiber composites. J Rheol 31:751–784

Archer L, Larson RG (1995) A molecular theory of flow alignment and tumbling in sheared nematic liquid crystals. J Chem Phys 103:3108–3111

Bandyopadhyay R, Basappa G, Sood AK (2000) Observation of chaotic dynamics in dilute sheared aqueous solutions of CTAT. Phys Rev Lett 84:2022–2025

Beris AN, Edwards BJ (1994) Thermodynamics of flowing systems with internal microstructure. Oxford Science Publications

Bird B, Armstrong RC, Hassager O (1987) Dynamics of polymeric liquids, vols 1 and 2. John Wiley and Sons

Burghardt WR (1998) Molecular orientation and rheology in sheared lyotropic liquid crystalline polymers. Macromol Chem Phys 199:471–488

Chaubal CV, Leal LG (1998) A closure approximation for liquid-crystalline polymer models based on parametric density estimation. J Rheol 42:177–201

Chaubal CV, Leal LG, Fredrickson GH (1995) A comparison of closure approximations for the Doi theory of LCPs. J Rheol 39:73–103

Chillingworth DRJ, Vicente Alonso E, Wheeler AA (2001) Geometry and dynamics of a nematic liquid crystal in a uniform shear flow. J Phys A 34:1393–1404

de Gennes PG, Prost J (1993) The physics of liquid crystals. Oxford University Press

Doi M (1981) Molecular dynamics and rheological properties of concentrated solutions of rodlike polymers in isotropic and liquid crystalline phases. J Polym Sci Polym Phys Ed 19:229–243

Doi M, Edwards SF (1986) The theory of polymer dynamics. Oxford University Press (Clarendon), London New York

Faraoni V, Grosso M, Crescitelli S, Maffettone PL (1999) The rigid-rod model for nematic polymers: an analysis of the shear flow problem. J Rheol 43:829–843

Farhoudi Y, Rey AD (1993) Shear flows of nematic polymers. I. Orienting modes, bifurcations, and steady state rheological predictions. J Rheol 37(2):289–314

Forest MG, Wang Q (2003) Monodomain response of finite-aspect-ratio macromolecules in shear and related linear flows. Rheol Acta 42:20–46

Forest MG, Wang Q, Zhou H (2000) Homogeneous pattern selection and director instabilities of nematic liquid crystal polymers induced by elongational flows. Phys Fluids 12(3):490–498

Forest MG, Wang Q, Zhou H (2001) On the flow-phase diagram for discotic liquid crystals in uniaxial extension and compression. Liq Cryst 28(5):717–720

Forest MG, Wang Q, Zhou H (2002a) Structure evolution in tumbling and kayaking nematic LCPs between shearing plates. http://www.amath.unc.edu/PAMPS

Forest MG, Zhou R, Wang Q (2002b) Symmetries of the Doi kinetic theory for nematic polymers of arbitrary aspect ratio: at rest and in linear flows. Phys Rev E 66(3):031712

Forest MG, Zhou R, Wang Q (2003a) Full-tensor alignment criteria for sheared nematic polymers. J Rheol 47(1):105–127

Forest MG, Zhou R, Wang Q (2003b) Scaling behavior of kinetic orientational distributions for dilute nematic polymers in weak shear. http://www.amath.unc.edu/PAMPS. J Non-Newt Fluid Mech (to appear)

Forest MG, Wang Q, Zhou R (2003c) Nematic polymer torque dynamics: multi-scale analogies, http://www.amath.unc.edu/PAMPS

Fuller GG (1995) Optical rheometry of complex fluids. Oxford University Press, Oxford

Gear CW, Kevrekidis IG, Theodoropoulos C (2003) Coarse integration/bifurcation analysis via microscopic simulators: micro-Galerkin methods. Comput Chem Eng (submitted)

Grosso M, Keunings R, Crescitelli S, Maffettone PL (2001) Prediction of chaotic dynamics in sheared liquid crystalline polymers. Phys Rev Lett 86(14):3184–3187

Hess S (1976) Fokker-Planck-equation approach to flow alignment in liquid crystals. Z Naturforsch Teil 31A:1034

Hinch EJ, Leal LG (1976) Constitutive equations in suspension mechanics. Part 2. Approximate forms for a suspension of rigid particles affected by Brownian rotations. J Fluid Mech 76(11):187–208
Kiss G, Porter RS (1978) Rheology of concentrated solutions of poly(γ-benzyl-glutamate). J Polym Sci Polym Symp 65:193
Kiss G, Porter RS (1980) Rheology of concentrated solutions of helical polypeptides. J Polym Sci, Polym Phys Ed 18:361
Kroger M, Sellers HS (1995) Viscosity coefficients for anisotropic, nematic fluids based on structural theories of suspensions. J Chem Phys 103:807–817
Kuzuu N, Doi MJ (1983) Constitutive equation for nematic liquid crystals under weak velocity gradient derived from a molecular kinetic equation. Phys Soc Jpn 52:3486–3494
Kuzuu N, Doi MJ (1984) Constitutive equation for nematic liquid crystals under weak velocity gradient derived from a molecular kinetic equation. II. Leslie coefficients for rodlike polymers. Phys Soc Jpn 53:1031–1040
Larson RG (1990) Arrested tumbling in shearing flows of liquid crystal polymers. Macromolecules 23:3983–3992
Larson RG (1999) Rheology of complex fluids. Oxford University Press
Larson RG, Ottinger H (1991) The effect of molecular elasticity on out-of-plane orientations in shearing flows of liquid crystalline polymers. Macromolecules 24:6270–6282
Maffettone PL, Crescitelli S (1995) Bifurcation analysis of a molecular model for nematic polymers in shear flows. J Non-Newtonian Fluid Mech 59:73–91
Maffettone PL, Sonnet AM, Virga EG (2000) Shear-induced biaxiality in nematic polymers. J Non-Newtonian Fluid Mech 90:283–297
Magda JJ, Baek SG, DeVries KL, Larson RG (1991) Shear flows of liquid crystal polymers: measurements of the second normal stress difference and the Doi molecular theory. Macromolecules 15:4460–4468
Marrucci G (1991) Tumbling regime of liquid crystalline polymers. Macromolecules 24:4176–4182
Marrucci G, Greco F (1991) The elastic constants of Maier-Saupe rodlike molecular nematics. Mol Cryst Liq Cryst 206:17–30
Marrucci G, Greco F (1993) Flow behavior of liquid crystalline polymers. Adv Chem Phys 86:331–404
Marrucci G, Maffettone PL (1989) Description for the liquid crystalline phase of rodlike polymers at high shear rates. Macromolecules 22:4076–4082
Mather PT, Pearson DS, Larson RG (1996a) Flow patterns and declination-density measurements in sheared nematic liquid crystals. I. Flow-aligning 5CB. Liq Cryst 20(5):527–538
Mather PT, Pearson DS, Larson RG (1996b) Flow patterns and declination-density measurements in sheared nematic liquid crystals. II. Tumbling 8CB. Liq Cryst 20(5):539–546
Messiah A (1961) Quantum mechanics, vol 2. North-Holland Publishing Company, Amsterdam
Mewis J, Mortier M, Vermant J, Moldenaers P (1997) Experimental evidence for the existence of a wagging regime in polymeric liquid crystals. Macromolecules 30:1323–1328
Onogi S, Asada T (1980) Rheology and rheo-optics of polymer liquid crystal. In: Astria G, Marrucci G, Plenum N (eds) Rheology. New York
Rienacker G, Hess S (1999) Orientational dynamics of nematic liquid crystals under shear flow. Physica A 267:294–321
See H, Doi M, Larson RG (1990) The effect of steady flow: fields on the isotropic-nematic phase transition of rigid rod-like polymers. J Chem Phys 92(1):792–800
Semenov AN (1983) Rheological properties of a liquid crystal solution of rod-like molecules. Sov Phys JETP 58:321–326
Srinivasarao M, Berry GC (1991) Rheo-optical studies on aligned nematic solutions of a rodlike polymer. J Rheol 35:379–397
Tan Z, Berry GC (2003) Studies on the texture of nematic solutions of rodlike polymers. 3. Rheo-optical and rheological behavior in shear. J Rheol 47(1):73–104
Theodoropoulos C, Qian Y, Kevrekidis IG (2000) Proc Nat Acad Sci 97:9840–9843
Tsuji T, Rey AD (1997) Effect of long range order on sheared liquid crystalline polymers. Part 1. Compatibility between tumbling behavior and fixed anchoring. J Non-Newtonian Fluid Mech 73:127–152
Vicente Alonso E, Wheeler AA, Sluckin TJ (2003) Nonlinear dynamics of a nematic liquid crystal in the presence of a shear flow. Proc R Soc A (submitted)
Wang Q (1997) Biaxial steady states and their stability in shear flows of liquid crystal polymers. J Rheol 41(5):943–970
Wang Q (2002) A hydrodynamic theory for solutions of nonhomogeneous nematic liquid crystalline polymers of different configuration. J Chem Phys 116(20):9120–9136